

Virtual Special Issue Coastal ocean modelling

Description of surface transport in the region of the Belizean Barrier Reef based on observations and alternative high-resolution models



D. Lindo-Atichati^{a,b,c,*}, M. Curcic^d, C.B. Paris^d, P.M. Buston^e

^a City University of New York, College of Staten Island, Department of Engineering Science and Physics, Staten Island, NY 10314, USA

^b Graduate Center of the City University of New York, Doctoral Program in Earth and Environmental Sciences, New York, NY 10016, USA

^c Department of Applied Ocean Physics and Engineering, Woods Hole Oceanographic Institution, Woods Hole, MA USA

^d University of Miami, Rosenstiel School of Marine and Atmospheric Science, Miami, FL 33149, USA

^e Boston University, Department of Biology and Marine Program, Boston, MA 02215, USA

ARTICLE INFO

Article history:

Received 5 June 2015

Revised 16 September 2016

Accepted 17 September 2016

Available online 20 September 2016

Keywords:

Ocean-atmosphere model

Lagrangian drifters

High-resolution

Coral reefs

Belize

ABSTRACT

The gains from implementing high-resolution versus less costly low-resolution models to describe coastal circulation are not always clear, often lacking statistical evaluation. Here we construct a hierarchy of ocean-atmosphere models operating at multiple scales within a $1 \times 1^\circ$ domain of the Belizean Barrier Reef (BBR). The various components of the atmosphere-ocean models are evaluated with in situ observations of surface drifters, wind and sea surface temperature. First, we compare the dispersion and velocity of 55 surface drifters released in the field in summer 2013 to the dispersion and velocity of simulated drifters under alternative model configurations. Increasing the resolution of the ocean model (from $1/12^\circ$ to $1/100^\circ$, from 1 day to 1 h) and atmosphere model forcing (from $1/2^\circ$ to $1/100^\circ$, from 6 h to 1 h), and incorporating tidal forcing incrementally reduces discrepancy between simulated and observed velocities and dispersion. Next, in trying to understand why the high-resolution models improve prediction, we find that resolving both the diurnal sea-breeze and semi-diurnal tides is key to improving the Lagrangian statistics and transport predictions along the BBR. Notably, the model with the highest ocean-atmosphere resolution and with tidal forcing generates a higher number of looping trajectories and sub-mesoscale coherent structures that are otherwise unresolved. Finally, simulations conducted with this model from June to August of 2013 show an intensification of the velocity fields throughout the summer and reveal a mesoscale anticyclonic circulation around Grovers Reef, and sub-mesoscale cyclonic eddies formed in the vicinity of Columbus Island. This study provides a general framework to assess the best surface transport prediction from alternative ocean-atmosphere models using metrics derived from high frequency drifters' data and meteorological stations.

© 2016 Elsevier Ltd. All rights reserved.

1. Introduction

The coastal ocean is receiving significant attention due to an increasing exploitation of its resources worldwide (Pauly et al., 2013). Knowledge of the coastal circulation is useful for many applications, from assessment of pollution risk to management of nearshore fisheries. For example, transport in the coastal ocean drives the exchange of larval fish among populations and influences the population dynamics and genetic structure of marine

species (Paris et al., 2007; D'Aloia et al., 2013; D'Aloia et al., 2014). Consequently, it is important to predict patterns of dispersal and population connectivity to manage fisheries and design effective networks of reserves (Sala et al., 2002; Fogarty and Botsford, 2007; Almany et al., 2009). Although management strategies might benefit from considering coastal circulation, observations of currents and coastal circulation models are scarce for most reef ecosystems.

Development of ocean circulation models has proceeded rapidly over the last 25 years. Progress has been made in three key areas. First, the number and spatial extent of models has increased: models now predict transport at coastal, basin, and global scales (Hurlburt and Hogan, 2000). Second, the horizontal resolution of models has increased: models with fine resolutions are now able

* Corresponding author at: City University of New York, College of Staten Island, Department of Engineering Science and Physics, Staten Island, NY 10314, USA.

E-mail addresses: david.lindo@csi.cuny.edu, dlindo@whoi.edu (D. Lindo-Atichati).

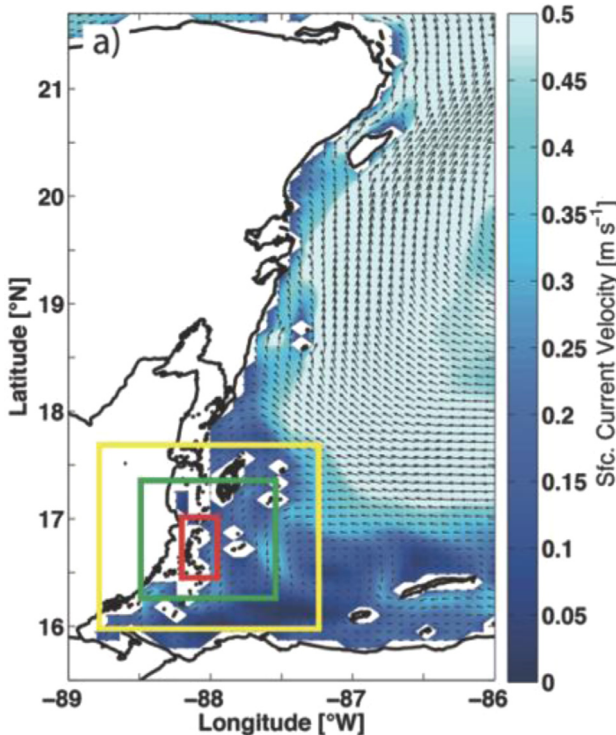


Fig. 1. Map showing the Belizean Barrier Reef System and the rest of the Meso-American Barrier Reef System, with surface ocean currents from GLB-HYCOM on 12 November 2012 showing the Caribbean Current in light blue, domain of the atmospheric (yellow square) and ocean (green square) models, and the 40 km stretch where drifters are deployed (red rectangle). (For interpretation of the references to colour in this figure legend, the reader is referred to the web version of this article.)

to resolve eddies and instabilities in the ocean (Luettich et al., 1992; Shchepetkin and McWilliams, 2005). Third, the vertical resolution of models has increased: models can use uniform depth levels (z-level models) (Griffies et al., 2005), density as a vertical coordinate (Bleck, 2002), or terrain-following (sigma or s-coordinate) structure (Ezer et al., 2002). Curiously, despite these advances, the gains made by increasing the resolution of the models are not well understood because i) the predictive skill of alternative models with different spatio-temporal resolution is rarely compared and ii) the mechanistic cause of the difference in predictive skill is rarely investigated.

One reef ecosystem that is experiencing increased utilization of its resources is the Belizean Barrier Reef System (BBRS) (Fig. 1). The BBRS stretches from Honduras through Belize to Mexico, and it is the longest (ca. 1000 km) barrier reef in the Western Hemisphere. The BBRS separates the coastal domain in two different regions: a) a shallow lagoon located shoreward of the reef, between the reef and the coastline, to the west; and b) a region of steep walls and oceanic waters seaward of the reef, to the east. Thirteen marine protected areas have been established on the Belizean portions of the BBRS (Cho, 2005) and offshore oil exploration is currently being considered (Cisneros-Montemayor et al., 2013). A coastal circulation model would facilitate management of this ecologically and economically important region (Cooper et al., 2009).

The main mesoscale circulation features in the region of the BBRS are the Caribbean Current and a cyclonic circulation in the Gulf of Honduras (Fig. 1). In situ hydrographic measurements suggest that the BBRS circulation can be divided into two distinct regimes, a northern BBRS region that acts as a boundary between the northward-flowing Yucatan Current and the rest of the BBRS, and a southern BBRS region with weaker southward coastal currents and the presence of the Honduras Gyre (Carrillo et al., 2015).

Satellite observations of ocean color suggest that there are significant land-reef connections in the BBRS (Soto et al., 2009), and in situ observations suggest that the strength of currents are controlled partially by tidal forcing at the northern and southern end of atolls in Belize (McClanahan and Karnauskas, 2011). Existing models suggest that when cyclonic eddies are present near the BBRS they cause a reinforced cyclonic circulation and flow is predominantly southward along the reef (Ezer et al., 2005; Chérubin et al., 2008); conversely, when anticyclonic eddies are present near the BBRS they cause a weakened cyclonic circulation and flow is predominantly westward across the reef (Ezer et al., 2005; Chérubin et al., 2008).

In contrast to what is known about mesoscale circulation features, little is known about the sub-mesoscale ocean features in the region. Sub-mesoscale features are characterized by horizontal scale smaller than internal Rossby radius of deformation. The averaged first-baroclinic Rossby radius of deformation R_1 within the BBRS is approximately 65 km (Chelton et al., 1998). Capturing the sub-mesoscale dynamics requires horizontal resolutions in the ocean models to be at least an order of magnitude smaller than the first-baroclinic Rossby radius of deformation. Our understanding of the coastal circulation in the region of the BBRS would be advanced by implementing a high-resolution ocean-atmosphere model that accounts for: a) sub-mesoscales where the flow departs from geostrophic balance; b) non-linear flow-topography interactions (Ezer et al., 2012); and c) tidal fluctuations.

The main aim of the present work is to prescribe an ocean-atmosphere model for the BBRS. For this purpose, we implement alternative models with various resolutions and forcing, and evaluate them by their ability to predict initial surface transport of drifters along the BBR. The performance of the alternative models is further assessed using surface wind, sea surface temperature from meteorological stations, and satellite derived sea surface temperature. The discrepancies among the models are investigated in more detail to understand the processes that need to be resolved for accurate predictions. Finally, we use the best model configuration to describe the surface flow of the region during the summer of 2013 when the observations were made.

2. Methods: in situ observations and modeling

2.1. In situ drifters, flow description, and meteorological stations

The primary dataset used in this work is from surface drifters provided by the Consortium for Advanced Research on Transport of Hydrocarbon in the Environment (CARTHE, <http://carthe.org>). The drifters are drogued at 40 cm and designed to sample the near-surface current while minimizing windage. They are tracked using Global Positioning System (GPS) every second with 5 m accuracy. The GT-31 GPS receivers are set in a waterproof housing attached to the drifter (MacMahan et al., 2009).

From May 30 to July 2 of 2013, 55 drifter deployments were made at 1–5 km off a 40 km stretch of the BBR centered on South Water Caye (16.82°N, 87.97°W) (Fig. 2b and c, red rectangles). This deployment region of about 400 km² was chosen to describe the circulation near the coral reefs for subsequent integration with larval dispersal data (D'Aloia et al., 2015). Thirty five percent of the drifters were deployed shoreward of the reef and 65% seaward of the reef at isobaths deeper than 50 m where the circulation can differ from that in the lagoon. The drifter deployments targeted different tidal phases with 27 drifters deployed on flood, 13 drifters on ebb, and 15 drifters on slack tidal phases. Most of the deployments involved clusters of 2 drifters at a single location, with initial separation of less than 500 m, to calculate dispersion. The mean duration of each deployment was 2.4 ± 0.8 h. The time series of drifter positions is used to derive the four following metrics

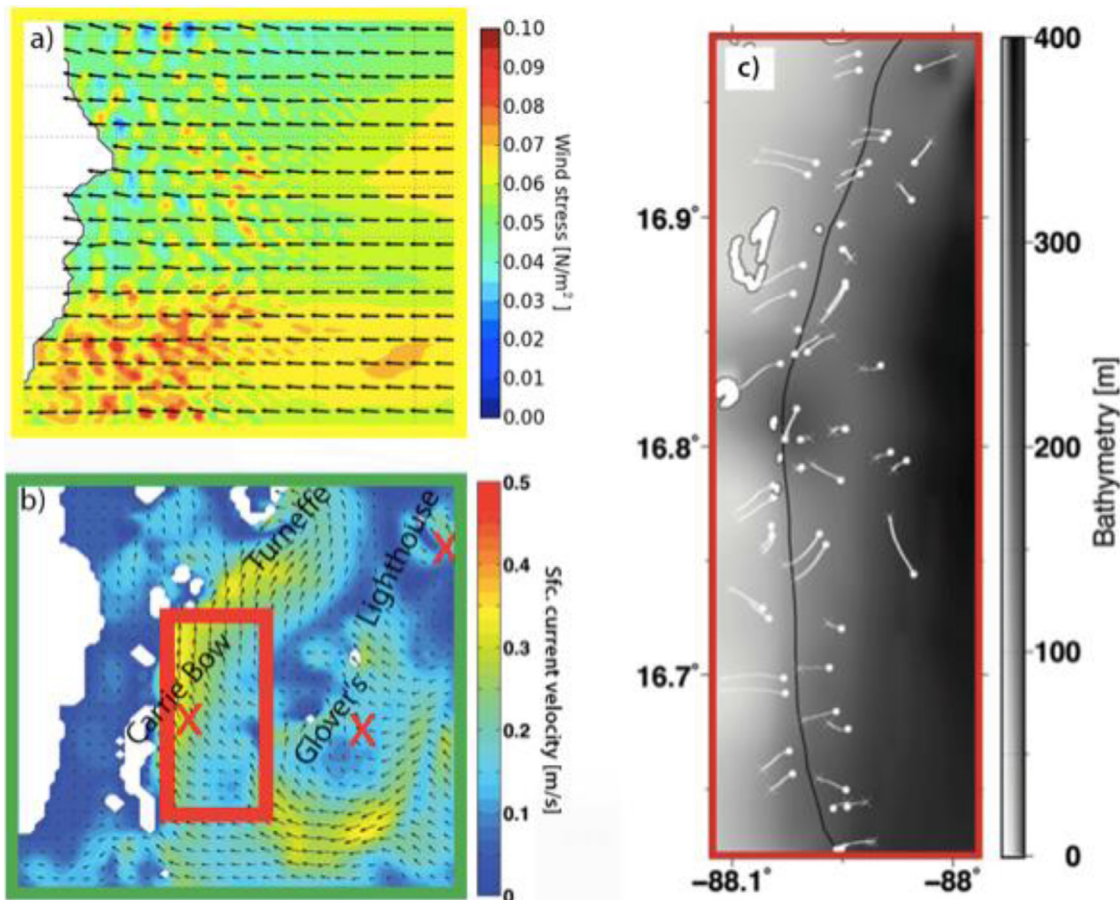


Fig. 2. (a) Wind stress field at sea surface predicted by WRF. (b) Current velocity field at sea surface predicted by BBR-HYCOM, 40 km stretch where drifters are deployed (red rectangle), and location of the three meteorological stations used for model validation (red crosses). In a and b, color contours and black arrows indicate magnitudes and vectors of wind stress [N m^{-2}] and current velocity [m s^{-1}] respectively (Both predictions taken on 18 May 2013 at 11:00 am). (c) Drifter tracks used in this study: white dots denote launch positions and white crosses denote final positions. (For interpretation of the references to colour in this figure legend, the reader is referred to the web version of this article.)

describing the Lagrangian flow along the 40 km stretch along the reef: 1) direction of the drifters merged to 45° octants; 2) u velocity component; 3) v velocity component; and 4) relative dispersion. The velocity components provide a description of the speed, direction and ultimately position of particles for comparison with the models.

We measure relative dispersion as the squared separation distance D between trajectories:

$$D^2(t) = \frac{1}{n} \sum_{i \neq j} |x_i(t) - x_j(t)|^2 \quad (1)$$

where $x_i(t)$ gives the time dependent vector position of the pairs of drifters i and j, and the sum is over all drifter pairs n (Ohlmann et al., 2012). Relative dispersion provides a description of the spreading of fluid particles under advection and turbulent motions for comparison with the models.

To describe the surface flow and test for differences between the velocity components of surface drifters in different regions (seaward versus shoreward) and different tidal phases (ebb versus flood), we conduct two Mixed Model (MM) analyses (West et al., 2006). MM is a statistical model containing both fixed effects and random effects. In each analysis the response variable is the observed velocity (e.g., observed u) and the predictor variables are the location of the drifter (seaward or shoreward) and the tidal phase (ebb or flood) at each time. To control for the lack of independence between data points from the same release, we use the release identification number as a random effect.

To describe the surface flow and test for differences in the evolution of D^2 seaward versus shoreward and on ebb and flood tides, we perform a repeated measures permutational multivariate analysis of variance (RM-PERMANOVA; Anderson, 2001). Primer 6 software (Clarke and Gorley, 2006) is used to run permutations for the null hypothesis of no difference between the two time series.

Data from three meteorological stations are used to evaluate predictions of sea surface temperature and predictions of winds of alternative models (Fig. 2b). First, observations of sea surface temperature are obtained from the Glover's Atoll meteorological station located at 16.83°N , 87.78°W . This station is operated by the NOAA's Integrated Coral Observing Network (ICON) and delivered by the Coral Health and Monitoring Program (CHAMP) Portal. Second, observations of sea surface temperature are obtained from the Lighthouse Atoll meteorological station located at 17.19°N , 87.52°W . This station is operated by the NOAA's ICON and delivered by the CHAMP Portal. Third, observations of 10-m wind are obtained from the Carrie Bow Caye meteorological station located at 16.80°N , 88.08°W . This station is operated by the Smithsonian National Museum of Natural History.

2.2. The atmospheric model

The BBR is a coastal and shallow water system, so part of the ocean circulation is governed by alternating onshore and offshore diurnal wind forcing and radiative heating in shallow water. To generate the high-resolution atmospheric forcing fields for

the BBR, we use the non-hydrostatic Weather Research and Forecasting (WRF) with the Advanced Research WRF dynamical core (WRF-ARW, Skamarock and Klemp, 2008) atmospheric model, configured at $1/100^\circ$ (~ 1 km) horizontal resolution with 36 vertical levels (Fig. 2a). The WRF domain extends approximately 50 km beyond the domain of our ocean model to provide a buffer zone between boundary conditions from GFS through WRF to our region (Fig. 1, yellow square). The surface and boundary layer dynamics are parameterized by the Monin-Obukhov theory (Monin and Obukhov, 1954) and the Yonsei University vertical mixing scheme (Hong et al., 2006), while the cumulus convection is explicitly resolved. Drag coefficient, which determines the air-sea momentum flux in the surface layer parameterization, is based on laboratory measurements by Donelan et al. (2004). Cloud microphysics processes are parameterized using the single-moment, 5-species model WSM5 (Hong et al., 2004). WRF provides hourly fields of momentum, enthalpy and radiative fluxes, as well as precipitation as surface forcing to the ocean model. Initial and boundary conditions are provided by the National Center for Environmental Prediction (NCEP) Global Forecasting System (GFS) final analysis fields (NCEP-FNL). GFS is a global atmospheric model providing 6-hourly fields at $1/2^\circ$ horizontal resolution. We initialize WRF on 1 May 2013 and integrate the solution forward for 4 months. While the solution is constrained by the FNL boundary conditions that provide the synoptic flow from the environment, the WRF simulation provides realistic atmospheric flow that is governed by strong diurnal oscillations. Ocean feedback processes to the atmosphere are not considered in this study.

2.3. The ocean models

In order to accurately represent the complex coastal bathymetry that is characterized by small atolls, shallow lagoons, and steep walls, we use bathymetry data made by merging three data sources of 500 m resolution: (1) World Resources Institute (WRI) bathymetry from Millennium Coral Reef Mapping Project (Andréfouët et al., 2006) for the entire BBR-HYCOM domain; (2) depth measurements from an autonomous underwater vehicle (Shcherbina et al., 2008) for the outer shelf of Glover's Atoll; and, (3) in situ measurements using a depth sounder for the area within the lagoon of Glover's Atoll (Karnauskas et al., 2012).

Once the gridded high-resolution bathymetry is generated, initial and lateral boundary conditions are provided by the coarser resolution ($1/12^\circ$) global data-assimilated HYbrid Coordinate Ocean Model (HYCOM, Bleck, 2002; Chassignet et al., 2003; Wallcraft et al., 2009) (GLB-HYCOM hereafter). This simulation uses the Navy Coupled Ocean Data Assimilation (NCODA) system (Cummings, 2005) to assimilate sea surface height and sea surface temperature measurements, as well as available in situ profiles. HYCOM is implemented on a $1 \times 1^\circ$ domain ($16.35\text{--}17.30^\circ\text{N}$, $87.48\text{--}88.47^\circ\text{W}$), encompassing the BBR, Glover's Atoll, the southern tip of Turneffe Atoll, the southern tip of Lighthouse Atoll, and the lagoon between the BBR and the coast (Fig. 2b).

The grid resolution of BBR-HYCOM is $1/100^\circ$ horizontally with 32 hybrid vertical layers, which are isopycnal in the open, stratified ocean, but use the layered continuity equation to make a dynamically smooth transition to a terrain-following coordinate in shallow coastal regions, and to z-level coordinates near the surface and/or un-stratified seas. Vertical mixing is calculated using a non-local K-profile parameterization (Large et al., 1994).

Finally, the presence of tides poses a challenge for the transport prediction because the interaction of tides and bathymetry can cause complex flow pattern (Rainville and Pinkel, 2006) and can excite vertical motions that take the form of internal waves near steep reefs (Ezer et al., 2011). The displacement amplitudes of internal tides can be greater than 50 m and the associated current

speeds greater than 2 m s^{-1} (Arbic et al., 2012). Internal tidal currents play a prominent role in shelf dynamics and particle dispersal (Carter et al., 2012; Leichter et al., 2003; Pineda et al., 2007). Therefore, it is critical to incorporate tidal forcing in one of our model configurations, test the model predictions against observations, and compare them with results of model configurations that do not include tides.

There are two sources of tidal forcing in HYCOM. First, the astronomical tidal forcing of the four largest semidiurnal constituents (M2, S2, N2, and K2) and the four largest diurnal constituents (K1, O1, P1, and Q1) are added to the HYCOM general circulation model. Second, the parameterized topographic internal wave drag scheme of Garner (2005) is modified in HYCOM as described in Arbic et al. (2010) to account for internal tides. The wave drag scheme parameterizes the drag on tidal flows resulting from the generation of unresolved small-vertical-scale internal waves by tidal flow over rough topography. With these adaptations, our tidal configuration of HYCOM generates both barotropic and internal tides amidst the eddying general circulation. The forcing is imposed without any data constraints. HYCOM has been used in the past as tidal model to test its accuracy on basin-scale and global-scale simulations (Arbic et al., 2012; Arbic et al., 2010; Buijsman et al., 2015; Shriver et al., 2012; Stammer et al., 2014). Here, a tide-permitting BBR-HYCOM is implemented and solutions are generated with and without tidal forcing.

2.4. The Lagrangian model

The ocean-atmosphere models provide estimates of 3-D currents, temperature and density to the Connectivity Modeling System (CMS; Paris et al., 2013). The CMS is a probabilistic, multi-scale biophysical model: probabilistic because individual particle attributes are drawn at random from biological or non-biological trait distributions; multi-scale because it moves particles using a nested-grid framework that is independent of the ocean models. The CMS provides a Lagrangian description of oceanic phenomena of advection, dispersion, and retention, and is an open-source biophysical model commonly used in the oceanography community (Qin et al., 2014; Snyder et al., 2014; Wood et al., 2014).

A stochastic component is added to the horizontal motion of particles to represent subgrid-scale motion unresolved by the model, following the random walk model (i.e., Markov process on the displacement) described by Griffa (1996). This is parameterized in the CMS using a horizontal eddy diffusivity K_h term that varies from $0.6 \text{ m}^2 \text{ s}^{-1}$ to $8 \text{ m}^2 \text{ s}^{-1}$ (Table 1) according to the spatial scales prescribed by the grid size (Okubo, 1971). Although Okubo's diagrams are used as a standard and commonly accepted method to calculate K_h other valid methods can be used. For example, eddy diffusivities are occasionally derived from in situ drifters (Veneziani et al., 2004). Still, drifter-derived diffusivities are usually compared with the original Okubo's diagrams (Paris et al., 2002; Manning and Churchill, 2006; Schroeder et al. 2011; Lynch et al., 2014; Poje et al., 2014; Curcic et al., 2016). Also, scale-dependent diffusivities from numerical simulations are in good agreement with Okubo's diagrams (Mensa et al., 2015). Given that estimating diffusivity is not the focus of this work and given the short time and space scales of our deployments and simulations, we estimated K_h using the Okubo's diagrams. While eddy mixing is explicitly treated in the turbulent closure of HYCOM, K_h represents stochastic motion in the Lagrangian equation and is scale-dependent (Richardson 1926; Poje et al. 2014; Mensa et al. 2015). The CMS uses a fourth order Runge-Kutta integration in both time and space and a fine tricubic interpolation of water properties to the position of the particle, which is adaptive depending on the proximity of the particle to land. Further details on the CMS application can be found in Paris et al. (2013).

Table 1

Summary of the models used in the drifter simulations. Horizontal diffusivities K_a are derived from the diffusion diagrams of Okubo (1971).

Model description (acronym)	Models used	Resolution	Frequency [h]	K_a [$m^2 s^{-1}$]	Tidal phase
Low-resolution Ocean and Low-resolution Atmospheric model (LOLA)	GLB-HYCOM + NOGAPS	1/12°, 1/2°	24, 6	8	Off
High-resolution Ocean model and Low-resolution Atmospheric model (HOLA)	BBR-HYCOM + NOGAPS	1/100°, 1/2°	1, 6	0.6	Off
High-resolution Ocean model and High-resolution Atmospheric model (HOHA)	BBR-HYCOM + WRF	1/100°, 1/100°	1, 1	0.6	Off
High-resolution Ocean model and High-resolution Atmospheric model with Tides (HOHAT)	Tidal BBR-HYCOM + WRF	1/100°, 1/100°	1, 1	0.6	On

2.5. Description of the alternative models

We set up the four following alternate ocean-atmospheric models to predicted surface transport:

- (1) A Low-resolution Ocean model and Low-resolution Atmospheric model (LOLA);
- (2) A High-resolution Ocean model and Low-resolution Atmospheric model (HOLA);
- (3) A High-resolution Ocean model and High-resolution Atmospheric model (HOHA);
- (4) A High-resolution Ocean model and High-resolution Atmospheric model with Tidal forcing (HOHAT).

The effect of the temporal and spatial resolution of the ocean model on predicted surface transport is addressed by comparing results from LOLA and HOLA experiments. The effects of the temporal and spatial resolution of the atmospheric model on predicted surface transport is studied by comparing results from HOLA and HOHA experiments. Atmospheric fields in HOLA and HOHA are fundamentally different in the sense that HOLA is based on analysis fields with some observations assimilated and thus represents actual weather systems, while HOHA is based on a very high-resolution free-running simulation that is only constrained by boundary conditions. Thus, we can expect HOLA to better represent synoptic weather systems on longer time scales, while HOHA is likely to better represent small-scale processes on diurnal time scales. Finally the role of tidal forcing in the ocean model on predicted surface transport is investigated by comparing results from HOHA and HOHAT experiments (Table 1).

To test the hypothesis that high-resolution ocean circulation is necessary to predict drifter trajectories accurately, we used an existing low-resolution model (LO) and implemented a high-resolution ocean model (HO). The low-resolution ocean model is based on the 0.08° resolution, data-assimilated GLB-HYCOM analysis fields. The high-resolution ocean model is the 0.01° resolution BBR-HYCOM simulation. To compare both ocean models, the same atmospheric forcing was needed (LA). Because GLB-HYCOM uses the 42-km resolution Navy Operational Global Atmospheric Prediction System (Hogan and Rosmond, 1991) winds and surface fluxes (NOGAPS hereafter), Both LOLA and HOLA experiments use atmospheric forcing fields from NOGAPS.

To test the hypothesis that tidal forcing is necessary to predict drifter trajectories accurately, we implemented a high-resolution ocean model (HO) with and without tidal forcing (T). The high-resolution ocean models were based on the BBR-HYCOM. To compare both ocean models, the same atmospheric forcing was needed (HA). We used the high-resolution atmospheric model based on WRF, as described in Section 2.2.

The three-dimensional current velocity data provided by each of the four model configurations (LOLA, HOLA, HOHA, and HOHAT) is delivered to the CMS to simulate Lagrangian particles released at the same time and place as the real drifters. Because ocean currents are highly variable both spatially and temporally and because sub-mesoscale flows are chaotic in nature, two particles deployed

simultaneously at slightly different locations often follow very different paths and their separation distance grows rapidly with time (LaCasce et al., 2008). Because of this, a single predicted Lagrangian trajectory can be considered as a stochastic realization from an envelope of possible trajectories (Brankart 2013). Also, because of the inherent chaotic nature of nonlinear advection (Klocker and McDougall, 2010) it is only in a statistical sense that the modeled flows can be compared to the real world flows (Mariano et al., 2002). Such indeterminacy necessitates a statistical or probabilistic description inferred from ensembles of trajectories (LaCasce et al., 2008). To account for this indeterminacy and for the unresolved subgrid-scale processes in the ocean model, we release 100 particles at each location where a drifter was released (Graham et al., 2002; Lynch et al., 2014), and thus produce an envelope of likely trajectories. Particles are tracked for 5 h using the integration time step of 30 s and 5500 trajectories (100 particles × 55 locations) are calculated. Pathways of modeled trajectories are terminated when reaching a shoreline boundary just as drifter observations terminate when they beach. The mean velocity components (u and v) of all simulated particle at each time step are compared to the velocity components of the drifter at each time step. The mean trajectory of each set of 100 particles is calculated, the modeled dispersion of pairs of mean trajectories drifters is computed at each time step, and compared to the observed dispersion of the corresponding pairs of drifters at each time step.

2.6. Model evaluation and statistical analyses

We used four metrics for comparison of model predictions and observations. We used u velocity component, v velocity component, and relative dispersion for comparison of simulated and real drifters, and satellite derived sea surface temperature for comparison of simulated and observed sea surface temperature. Frequency distributions of differences between simulated and observed drifter velocity components are calculated for LOLA, HOLA, HOHA, and HOHAT. Time series of relative dispersion are calculated for the pairs of drifters and for the pairs of Lagrangian particles from LOLA, HOLA, HOHA, and HOHAT. Frequency distributions of differences between simulated and observed sea surface temperatures are calculated for LOLA, HOLA, HOHA, and HOHAT. To test the differences in the frequency distribution of differences in velocities, differences in the evolution of D^2 we conducted the RMPERMANOVA analysis.

To explore potential causes of the differences between predictions of models of different resolution and to better understand the dynamics of the sub-mesoscale and mesoscale eddy fields we used a quantitative method of looper identification (Veneziani et al., 2004, 2005a, 2005b). The direct effect of coherent structures, such as rings, sub-mesoscale coherent vortices, and large-amplitude meanders, is to produce two distinct categories of drifter trajectories (Richardson et al., 1993). The loopers are quickly rotating drifters that are trapped inside highly energetic eddies, while the non-loopers represent the rest of trajectories, which experience little looping behavior, and are typically associated with the less ener-

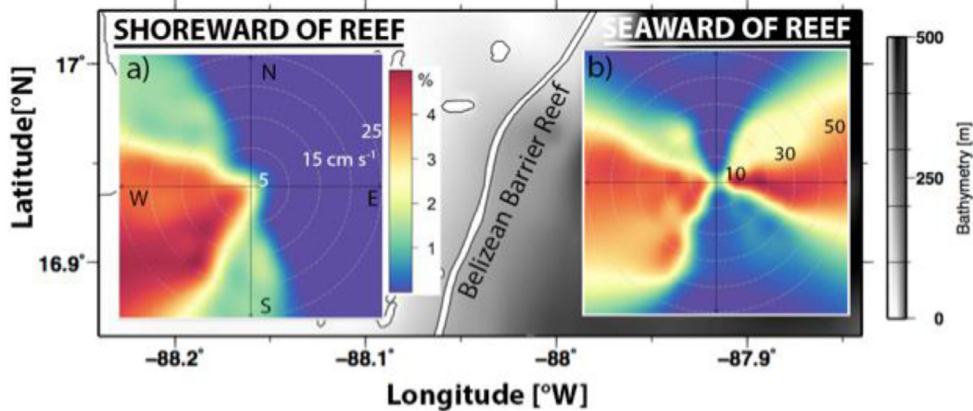


Fig. 3. Bivariate polar plots of percentage of drifters using the mean Direction of Motion (DoM) and mean speed [cm s^{-1}] for real drifters deployed (a) shoreward and (b) seaward of the reef.

getic background flow. This criterion results in a distribution non-loopers and loopers (cyclonic and anticyclonic) presented in number of drifter days.

To explore the independent effect of tides on direction and speed of surface drifters we used bivariate polar graphs. Working in polar coordinates helps to understand the directional surface transport dependence of different models and locations. For example, these graphs show how the drifters' direction of motion and speed varied shoreward and seaward of the reef during the in situ experiments and how they vary in the Lagrangian simulations under different forcing fields. A Generalized Additive Model (GAM) is used to derive smooth surfaces for all bivariate polar graphs using the 'openair' open source tools (Carslaw and Ropkins, 2012).

To explore potential causes of the differences between atmosphere model predictions and to better understand the diurnal sea-breeze cycle in the Belizean Barrier Reef we compared domain-averaged 10-m wind during June and July of 2013 based on HOLA, the low-resolution (42 km grid spacing) analysis fields from NO-GAPS, and those based on HOHA, the high-resolution (1 km grid spacing) non-hydrostatic WRF simulation described in Section 2.2.

To further validate model predictions with in situ observations we evaluated: 1) HOLA and HOHA winds from 12 to 31 August 2013 using the observations of 10-m wind from a meteorological station located in Carrie Bow Caye sea surface temperature (SST) predicted by LOLA, HOLA, HOHA and HOHAT from 1 June to 31 July 2013 using the available observations of the meteorological stations located in Glover's Atoll and Lighthouse. For each of our ocean-atmosphere models (LOLA, HOLA, HOHA, and HOHAT) we generated a frequency distribution of differences between the simulated and measured SST. To test differences in the frequency distribution differences in sea surface temperature we conducted RM-PERMANOVA.

3. Results

3.1. Description of the Lagrangian flow

Drifters deployed shoreward of the reef have a mean speed of $18 \pm 5 \text{ cm s}^{-1}$, with directions of motion (DoM) distributed in the south (12%), southwest (41%), west (35%), and northwest (12%) respectively (Fig. 3a). Drifters deployed seaward of the reef have a mean speed of $17 \pm 9 \text{ cm s}^{-1}$, with DoM distributed in the northeast (13%), east (23%), southeast (3%), southwest (23%), west (27%), and northwest (10%) respectively (Fig. 3b). Evaluation of the predicted speed and DoM of simulated drifters is presented in Section 3.2. These qualitative differences in observed speed and DoM of the drifters are borne out by the following statistical analyses.

The u component of velocity of drifters released shoreward of the reef is less (more negative) than that of drifters released seaward (MM analysis: $\text{df} = 52$, $F = 13$, $P = 0.0008$); the u component of velocity of drifters released on flood tide is less (more negative) than that of drifters released on ebb tide (MM analysis: $\text{df} = 32,396$, $F = 286$, $P < 0.0001$). The v component of velocity of drifters released shoreward of the reef is not significantly different from that of drifters released seaward (MM analysis: $\text{df} = 52$, $F = 2$, $P < 0.1390$); the v component of velocity of drifters released on flood tide is less (more negative) than that of drifters released on ebb tide (MM analysis: $\text{df} = 32,396$, $F = 170$, $P < 0.0001$).

Considering dispersion, time series of mean D^2 computed from all available drifter pairs (Fig. 4a) shows three qualitatively distinct regimes (Fig. 4b, solid black curve and dashed vertical lines) that are significantly different (RM-PERMANOVA: $p = 0.0001$). During the initial period (0–130 min) observed mean D^2 increases linearly with a slope of $0.0001 \text{ km}^2 \text{ min}^{-1}$, indicating that the drifters separate at a rate of 0.2 m min^{-1} . During the intermediate period (130–180 min) mean D^2 fluctuates and declines to its initial value, indicating that the drifters moved closer together. During the late period (180–220 min) mean D^2 increases exponentially with e-folding time of 24 min, indicating that the drifters almost double their separation distance in this period. Evaluation of the predicted D^2 of simulated drifters is presented in Section 3.2.

Considering the effect of release location on mean D^2 during the entire period (0–220 min) it was observed that mean D^2 seaward of the reef is greater than that shoreward of the reef (RM-PERMANOVA: $p < 0.0001$). Finally, considering the effect of release time on mean D^2 during the entire period (0–220 min) it was observed that mean D^2 on ebb tide is not significantly different from that on flood tide (RM-PERMANOVA: $p = 0.1152$).

3.2. Ocean-atmosphere model evaluation

For each of our ocean-atmosphere models (LOLA, HOLA, HOHA, and HOHAT) we generated a frequency distribution of differences between the simulated and real drifter velocities. All model configurations overestimate velocity components and show higher mean numerical discrepancies for v component ($v_{\text{anom}} = 13 \pm 30 \text{ cm s}^{-1}$) than for u component ($u_{\text{anom}} = 6 \pm 33 \text{ cm s}^{-1}$). All models show higher mean numerical discrepancies for v component seaward of the reef ($v_{\text{anom}} = 19 \pm 42 \text{ cm s}^{-1}$) than shoreward of the reef ($v_{\text{anom}} = 8 \pm 19 \text{ cm s}^{-1}$) for all model configurations. Likewise, all models show similar mean numerical discrepancies for u component seaward of the reef ($u_{\text{anom}} = 8 \pm 37 \text{ cm s}^{-1}$) to that shoreward of the reef ($u_{\text{anom}} = 4 \pm 30 \text{ cm s}^{-1}$). A global test indicates that there are significant differences in these frequency

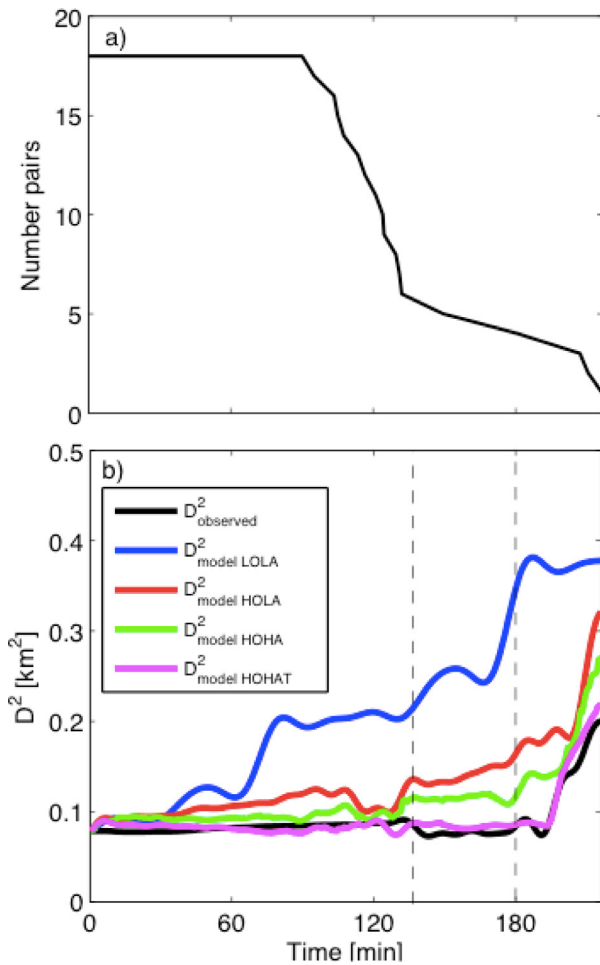


Fig. 4. Ensemble relative dispersion (D^2) of observed and simulated drifters. The number of available drifter pairs (a) is shown as a function of time since deployment. (b) Ensemble average D^2 of observed drifter pairs and ensemble average D^2 of Lagrangian particles pairs for different model configurations.

distributions for the four model configurations, for both u and v velocity components (RM-PERMANOVA: $p < 0.001$). Specifically, LOLA has the greatest anomalies ($u_{\text{anom}} = 10 \pm 62 \text{ cm s}^{-1}$, $v_{\text{anom}} = 20 \pm 64 \text{ cm s}^{-1}$), HOLA and HOHA show intermediate anomalies (HOLA: $u_{\text{anom}} = 7 \pm 35 \text{ cm s}^{-1}$, $v_{\text{anom}} = 17 \pm 24 \text{ cm s}^{-1}$; HOHA: $u_{\text{anom}} = 6 \pm 25 \text{ cm s}^{-1}$; $v_{\text{anom}} = 12 \pm 20 \text{ cm s}^{-1}$), while HOHAT has the smallest anomalies ($u_{\text{anom}} = 2 \pm 12 \text{ cm s}^{-1}$, $v_{\text{anom}} = 4 \pm 14 \text{ cm s}^{-1}$) (Fig. 5). Increasing the spatio-temporal resolution of the ocean model from $1/12^\circ$ and 24 h (LO) to $1/100^\circ$ and 1 h (HO) decreases the numerical discrepancies by 30% for u and decreases the v numerical discrepancies by 13%. Increasing the spatio-temporal resolution of the atmospheric model from $1/2^\circ$ and 6 h (LA) to $1/100^\circ$ and 1 h (HA) decreases the numerical discrepancies by 22% for u and decreases the v numerical discrepancies by 30%. Incorporating tidal forcing (T) to the model with spatio-temporal resolution of $1/100^\circ$ and 1 h (HOHA) decreases the numerical discrepancies by 65% for u and decreases the v numerical discrepancies by 67%.

The global test on the time series of D^2 (Fig. 4b) indicates that there are significant differences among model configurations (RM-PERMANOVA, global test: $p=0.001$), which are tested pairwise –LOLA vs. HOLA, HOLA vs. HOHA, and HOHA vs. HOHAT—for different time frames on Fig. 6. During the initial dispersion period (0–130 min), pairwise tests show that only LOLA is different from HOLA at $p < 0.05$. During the middle dispersion period (130–180 min) and late dispersion period (180–220 min), pairwise tests

show that LOLA is different from HOLA at $p < 0.05$, HOLA is different from HOHA at $p < 0.05$, and HOHA is different from HOHAT at $p < 0.05$. Increasing the spatio-temporal resolution of the ocean model from $1/12^\circ$ and 24 h (LO) to $1/100^\circ$ and 1 h (HO) decreases the D^2 numerical discrepancies by 63% during initial times, by 64% during intermediate times, and by 72% during late times. Increasing the spatio-temporal resolution of the atmospheric model from $1/2^\circ$ and 6 h (LA) to $1/100^\circ$ and 1 h (HA) has no significant effect on the D^2 numerical discrepancies during initial times, but decreases numerical discrepancies by 40% during intermediate times and by 45% during late times. Incorporating tidal forcing (T) to the model with spatio-temporal resolution of $1/100^\circ$ and 1 h (HOHA) has no significant effect on the D^2 numerical discrepancies during initial times, but decreases the D^2 numerical discrepancies by 40% during intermediate times and by 46% during late times.

All model configurations overestimate the observed SST for the time frame of our evaluation. For Glover's Atoll and Lighthouse Atoll respectively, LOLA has the greatest anomalies ($SST_{\text{anom}} = 1.52 \pm 0.16 \text{ }^\circ\text{C}$; $SST_{\text{anom}} = 1.72 \pm 0.2 \text{ }^\circ\text{C}$), while HOLA ($SST_{\text{anom}} = 0.81 \pm 0.28 \text{ }^\circ\text{C}$; $SST_{\text{anom}} = 0.78 \pm 0.3 \text{ }^\circ\text{C}$), HOHA ($SST_{\text{anom}} = 0.78 \pm 0.4 \text{ }^\circ\text{C}$; $SST_{\text{anom}} = 0.79 \pm 0.33 \text{ }^\circ\text{C}$), and HOHAT ($SST_{\text{anom}} = 0.77 \pm 0.27 \text{ }^\circ\text{C}$; $SST_{\text{anom}} = 0.82 \pm 0.33 \text{ }^\circ\text{C}$) show the smallest anomalies (Fig. 7). Increasing the spatio-temporal resolution of the ocean model from $1/12^\circ$ and 24 h (LO) to $1/100^\circ$ and 1 h (HO) significantly decreases the numerical discrepancies of SST by 46% at Glover's Atoll and 54% at Lighthouse (RM-PERMANOVA: $p < 0.001$). However, increasing the spatio-temporal resolution of the atmospheric model from $1/2^\circ$ and 6 h (LA) to $1/100^\circ$ and 1 h (HA), and incorporating tides (T) do not significantly affect the numerical discrepancies of SST.

One qualitative example of the ability of the models to synoptically represent the mesoscale SST patterns is provided in Fig. 8. Snapshots of Terra MODIS satellite SST (Fig. 8a) and Multi-scale Ultra-high Resolution (MUR) satellite analysis (Fig. 8b) for July 1 2013, indicate a strong sea surface temperature gradient that increases east to west. Model-derived SST from LOLA is a very uniform field and does not show this temperature gradient. However the model derived SST from HOLA, HOHA, and HOHAT are consistent with the strong zonal gradient of SST.

Finally, we validate the HOLA and HOHA winds from 12 to 31 August 2013 using the observations of 10-m wind from a meteorological station located in Carrie Bow Caye (Fig. 9). The overall synoptic patterns are better represented by NOGAPS analysis fields in HOLA, especially in the meridional component. While the observed diurnal variability is under-represented by both HOLA and HOHA, the high-resolution WRF simulation is more capable of capturing the local maxima in both zonal and meridional directions. We find that on average between 12 and 31 August, the RMS of the zonal diurnal component was 1.09, 1.57, and 2.69 m s^{-1} in case of HOLA, HOHA, and observations, respectively. For the meridional diurnal component, we find the RMS values of 1.09, 1.31, and 1.95 m s^{-1} in case of HOLA, HOHA, and observations, respectively.

3.3. Potential causes of differences in predictions of models

3.3.1. Mesoscale and sub-mesoscale looping trajectories

First, the four different models—LOLA, HOLA, HOHA, and HOHAT—are used to quantify differences in looping trajectories. These comparisons will provide insight on the number, polarity and spatial scale of ocean structures resolved by the models. Second, the high-resolution ocean-atmosphere models without and with tides—HOHA and HOHAT—are used to shed light on the effects of tides on surface transport shoreward and seaward of the reef.

Comparison of drifter simulations driven by the alternative models reveals that there is a significant difference

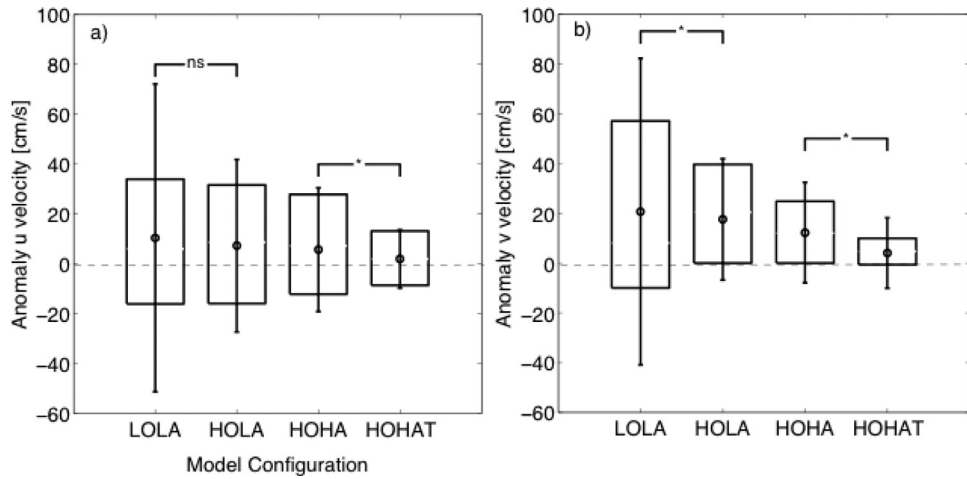


Fig. 5. Differences (anomalies) in u velocities and in v velocities between simulated and observed drifters under four model configurations. For LOLA, anomalies are calculated from 235 velocity differences; for HOLA, HOHA, and HOHAT anomalies are calculated from 32,400 velocity differences. The lower (upper) boundary lines of boxes are the 25% (75%) quantiles of the distributions. The central circles and vertical lines extending from the circles indicate mean and standard deviations of the distributions; ns, nonsignificant comparison; *, significant comparison.

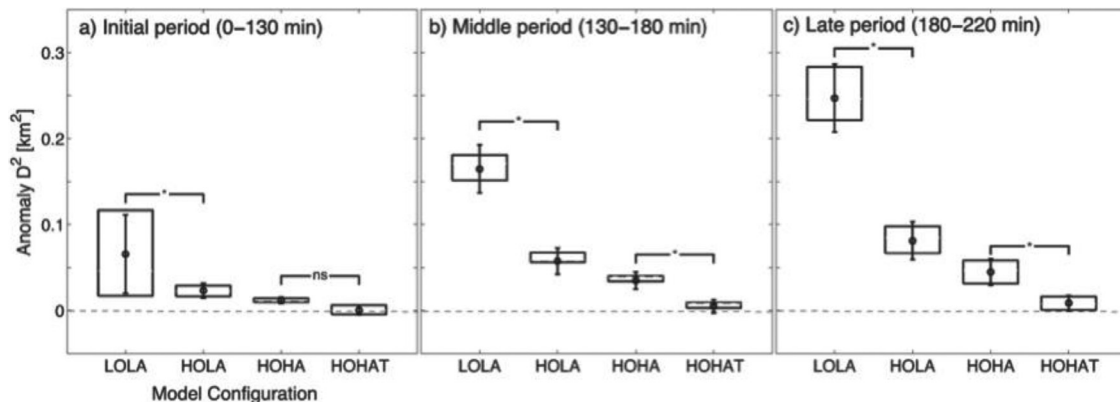


Fig. 6. Differences (anomalies) in relative dispersion (D^2) between simulated and observed drifters during (a) initial, (b) middle, and (c) late periods of dispersion under four model configurations. For LOLA, anomalies are calculated from 235 differences in D^2 ; for HOLA, HOHA, and HOHAT anomalies are calculated from 32,400 differences in D^2 . The lower (upper) boundary lines of boxes are the 25% (75%) ls of the distributions. The central circles and vertical lines extending from the circles indicate mean and standard deviations of the distributions; ns, nonsignificant comparison; *, significant comparison.

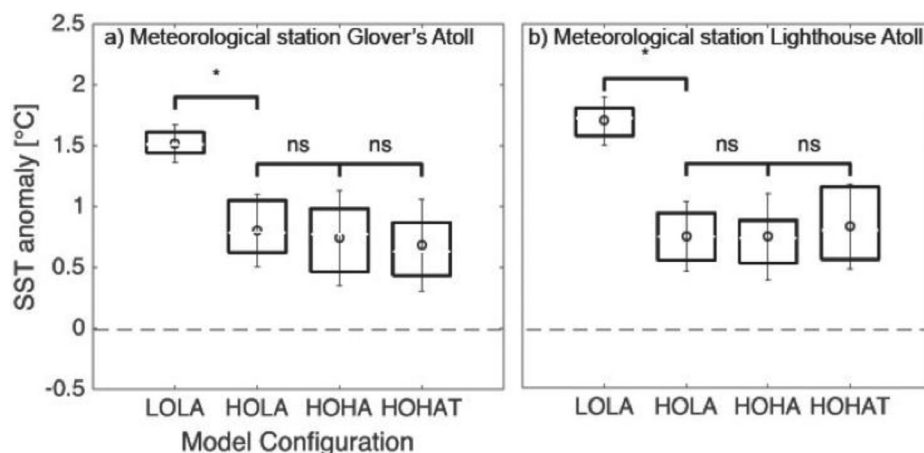


Fig. 7. Differences (anomalies) in sea surface temperature (SST) between model configurations and observations from meteorological stations at Glover's Atoll (a) and Turneffe Atoll (b) under four model configurations. Anomalies are calculated from 61 differences in SST for each model configuration and location, from June 1 to July 31 2013. The lower (upper) boundary lines of boxes are the 25% (75%) ls of the distributions. The central circles and vertical lines extending from the circles indicate mean and standard deviations of the distributions; ns, nonsignificant comparison; *, significant comparison.

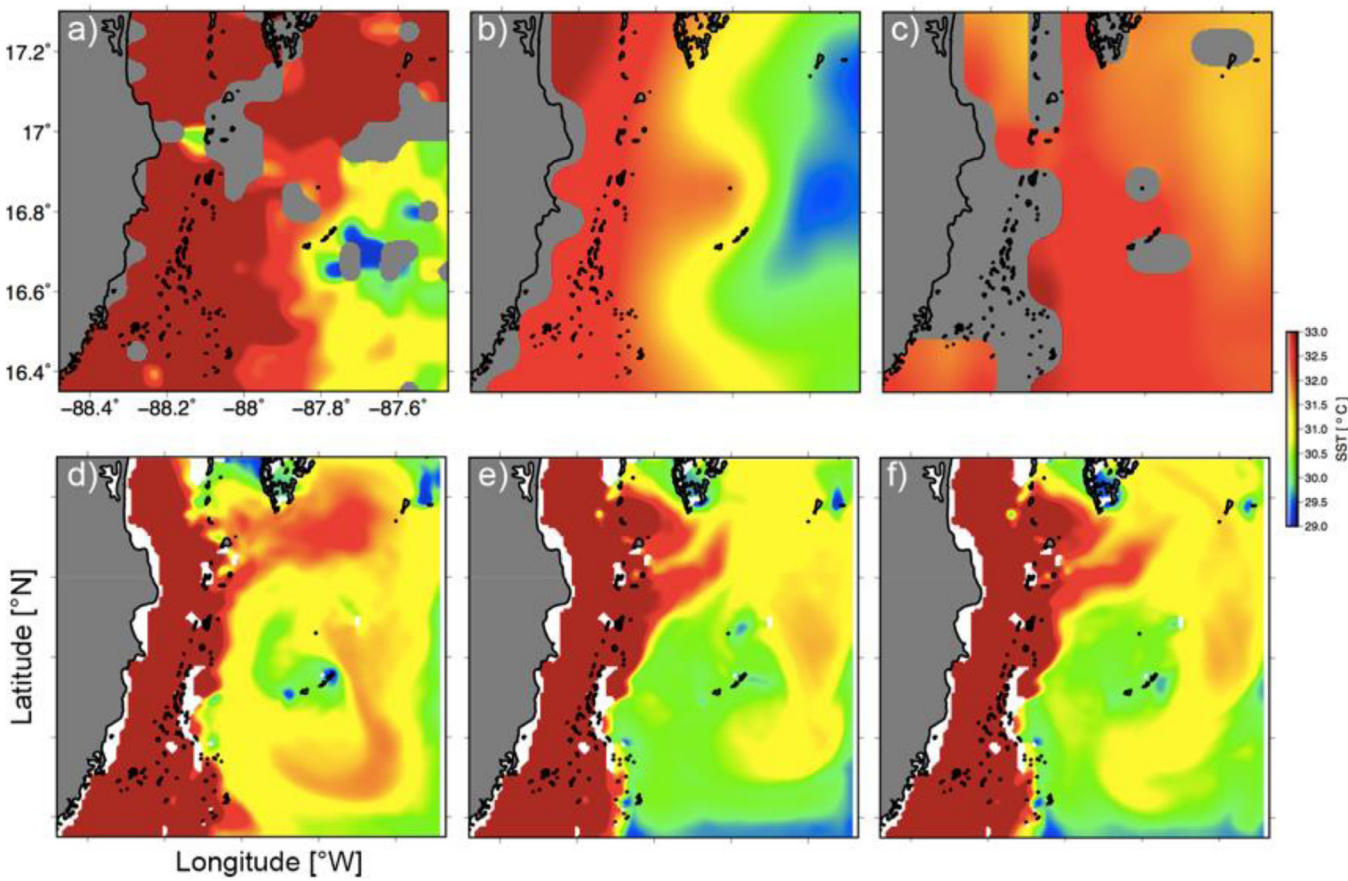


Fig. 8. Snapshots of SST from (a) Terra MODIS satellite, (b) Multi-scale Ultra-high Resolution (MUR) satellite analysis, (c) LOLA, (d) HOLA, (e) HOHA, and (f) HOHAT on July 1, 2013. The satellite SST (a–b) and high-resolution model SST (d–e) all indicate a strong zonal gradient of SST.

Table 2

Number of total Lagrangian trajectory data, nonlooping, and looping trajectory data in drifter days for the simulations of 100 drifters released at each of the same locations where in situ drifters were deployed for 4 months of high-resolution dispersal. The values in parenthesis (*) denote the number of sub-mesoscale looping trajectory data in drifter days. The loopers percentage is also in terms of days. Simulations are done for all model configurations.

Model	Total	Non-Looping	Looping			
			Cyclonic (*)	Anticyclonic (*)	Total (*)	% Looping (*)
LOLA	10,660	10,340	224 (0)	96 (0)	320 (0)	3 (0)
HOLA	43,460	39,114	2955 (591)	1391 (278)	4346 (869)	10 (2)
HOHA	68,060	53,767	9862 (5621)	4431 (2525)	14,293 (8147)	21 (12)
HOHAT	82,000	58,220	16,170 (13,583)	7610 (6392)	23,780 (19,975)	29 (24)

(RM-PERMANOVA, global test: $p < 0.001$) in the percentage of total (mesoscale and sub-mesoscale) looping trajectories generated by LOLA (3%) and that of HOLA, HOHA, and HOHAT (10%, 21%, and 29% respectively) (Table 2). Among these looping trajectories, all models predict approximately double number of drifter days in cyclonic eddies than in anticyclonic eddies. Noteworthy, there is a significant difference (RM-PERMANOVA, global test: $p < 0.001$) in the percentage of sub-mesoscale looping drifters among the models, with a highest percentage of sub-mesoscale looping trajectories (24%) found in HOHAT. Therefore the 83% of the total looping trajectories generated by HOHAT are in the sub-mesoscale range.

3.3.2. Tidal effect

Comparison of HOHA and HOHAT reveals that the presence of tides has a strong influence on drifters' mean direction of motion and mean speed (Fig. 10). The bivariate polar plots show

the direction of motion in polar coordinates and speed [cm s^{-1}] of drifters seaward and shoreward of the reef. The color of the plot indicates the percentage of drifters associated with each direction and speed for the deployed drifters (Fig. 10a and d), simulated drifters from the high-resolution ocean-atmosphere model (Fig. 10b and e), and simulated drifters simulated from the high-resolution ocean-atmosphere with tidal forcing model (Fig. 10c and f). The incorporation of tides in HOHAT improves the mean direction of motion and the mean speed of drifters predicted by HOHA. The improvement is specially marked shoreward of the reef. Note worthily, the incorporation of tidal forcing leads to a lower spatial distribution of mean direction of motion and mean speed of drifters than the model without tidal forcing.

3.3.3. Effects of diurnal sea-breeze on ocean currents

While the Meso-American region and the Caribbean Sea are subject to predominantly steady and moderate (typically

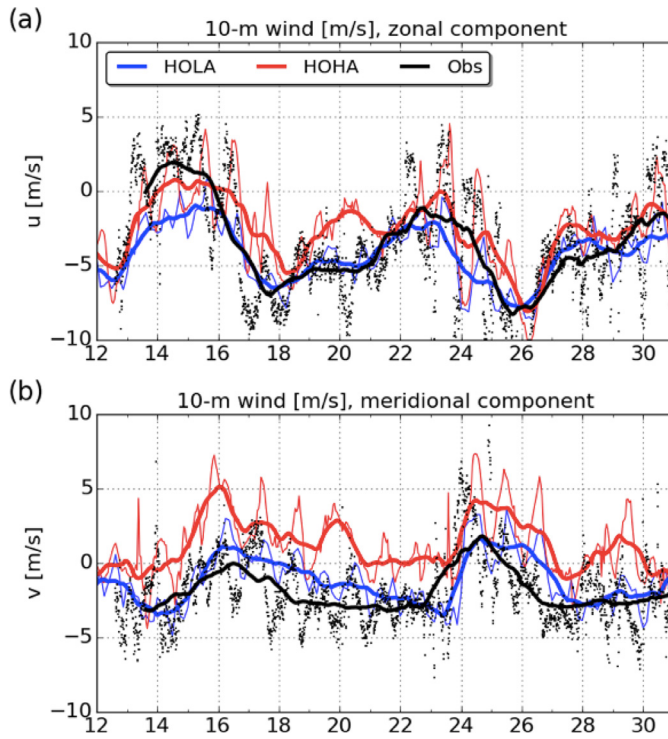


Fig. 9. Comparison between simulated and observed 10-m wind in (a) zonal and (b) meridional components, in case of HOLA (blue) and HOHA (red) configurations, at 16.80 N, 88.08 W, from 12 to 31 August 2013. Thin lines and dots correspond to actual values and measurements. Thick lines correspond to running-daily averages. (For interpretation of the references to colour in this figure legend, the reader is referred to the web version of this article.)

<15 m s⁻¹) easterly wind forcing during the summer, the circulation in the coastal area of the BBR is more complex because of the diurnal oscillations in the wind field. These oscillations are induced by the sharp land-sea contrast in the zonal direction and are characterized by alternating onshore (sea-breeze) and offshore (land-breeze) wind. [Lindo-Atchati and Sangrà \(2015\)](#) provided observational evidence of atmospheric modulation of the circulation in the eastern Gulf of Mexico. [Judit et al. \(2016\)](#) provided a comprehensive description of these flows and their impacts on the ocean in the Gulf of Mexico, as well as their variability between summer and winter seasons. Since the model representation of the land-sea contrast and resulting diurnal cycle are highly-dependent on grid resolution, it is imperative to understand the response of ocean circulation to atmospheric forcing of different resolutions.

We first compare 10-m wind fields from HOLA and HOHA experiments during June and July of 2013. To make the comparison representative of the whole coastal region, we average the wind fields over the whole BBR domain, excluding the 20 km band at the domain boundary. Compared to HOLA, we find that HOHA winds have an increased short-scale variability in both zonal and meridional components ([Fig. 11a, b](#)). The u-component of HOHA winds is similar to the NOGAPS analysis fields from HOLA on longer time scales, indicating that the free-running WRF simulation constrained by NCEP-FNL boundary conditions is capable of reproducing synoptic weather patterns months ahead. The meridional component of HOHA winds is larger than that of HOLA, possibly due to the slanted orientation of the coastline in the meridional direction ([Fig. 1](#)). Overall, the atmospheric circulation in the summer is predominantly easterly, with peak winds occasionally exceeding 10 m s⁻¹.

We further extract the diurnal cycle component by applying a running daily-average on the wind time series and subtracting

Table 3

Average 10-m wind and surface current, and the root-mean square (RMS) of their diurnal components in m s⁻¹, during June and July of 2013.

Component	Model	Mean wind	Diurnal wind RMS	Mean current	Diurnal current RMS
Zonal	HOLA	-3.81	1.38	-0.0724	0.0256
Zonal	HOHA	-4.42	1.44	-0.0442	0.0357
Meridional	HOLA	-1.99	1.00	0.0412	0.0270
Meridional	HOHA	0.61	1.26	0.0756	0.0344

from the total wind ([Fig. 11c, d](#)). Because the orientation of the coast is in the meridional direction, strongest diurnal cycle is found in the zonal component, and can exceed 4 m s⁻¹. Diurnal cycle in the meridional component is associated with the turning of the wind during the transition from sea-breeze to land-breeze (and vice versa), and is typically less than 2 m s⁻¹. Diurnal oscillations are strongest when the synoptic mean flow weakens and enables more organized convective motion that drives the sea-breeze ([Fig. 11a, c](#)). On average during June and July of 2013, HOHA had an enhanced diurnal cycle compared to HOLA by 4% and 26% in zonal and meridional components, respectively. In response, the ocean surface circulation in HOHA has a significantly larger variability on the diurnal time scales compared to HOLA ([Fig. 12](#)). Averaged over the same time period, HOHA surface currents exhibit 39% and 27% more diurnal variability in zonal and meridional components, respectively. The average wind and current velocities and the root-mean square diurnal components for HOLA and HOHA are given in [Table 3](#).

3.4. Modeled ocean circulation

The model that best predicts surface ocean currents and dispersion, HOHAT, is used to provide new insights into the surface ocean circulation in the region during the entire summer season of 2013. The monthly mean zonal velocities intensify from May through August ([Fig. 13](#)). In May and June, zonal velocities are weak, range from -0.2 to 0.1 m s⁻¹, and are predominantly negative in the southern region of the BBR domain south of Glover's Atoll ([Fig. 13a, b](#)). This is in agreement with the mean speed and mean DoM of drifters deployed along the reef in May and June 2013. In July and August, zonal velocities are moderate, range from -0.4 to 0.3 m s⁻¹, remain predominantly negative in the southern region of the BBR domain south of Glover's Atoll, and become predominantly positive in the northern region of the BBR domain between Glover's Atoll and Turneffe Atoll ([Fig. 13c, d](#)). The monthly mean meridional velocities also intensify from May through August ([Fig. 13](#)). In May and June, meridional velocities are weak, range from -0.1 to 0.25 m s⁻¹, are predominantly positive in the central region of the BBR domain between the reef Glover's Atoll and Turneffe Atoll, and are predominantly negative in the eastern region of the BBR domain east of Glover's Atoll ([Fig. 13a, b](#)). In July and August, meridional velocities are moderate, range from -0.25 to 0.4 m s⁻¹, become more positive in the western region of the BBR domain west of Glover's Atoll, and become more negative in the eastern region of the BBR domain east of Glover's Atoll. Noteworthily, the combined analysis of zonal and meridional velocities depict a clear signal of an anticyclonic circulation around Glover's Atoll that emerges in July and peaks in August.

The high-resolution spatial (~1 km) and temporal (1 h) evolution of mesoscale and sub-mesoscale ocean features is tracked along transects at 17.1°N, 16.65°N, 88°W, and 87.55°W ([Fig. 13d](#), dotted lines). This is explored with the Hovmöller diagrams of [Fig. 14](#), which show the evolution of sea surface height anomaly (SSHA) along these transects from 1 May to 31 August 2013. The mesoscale circulation along the four transects evolves from a cy-

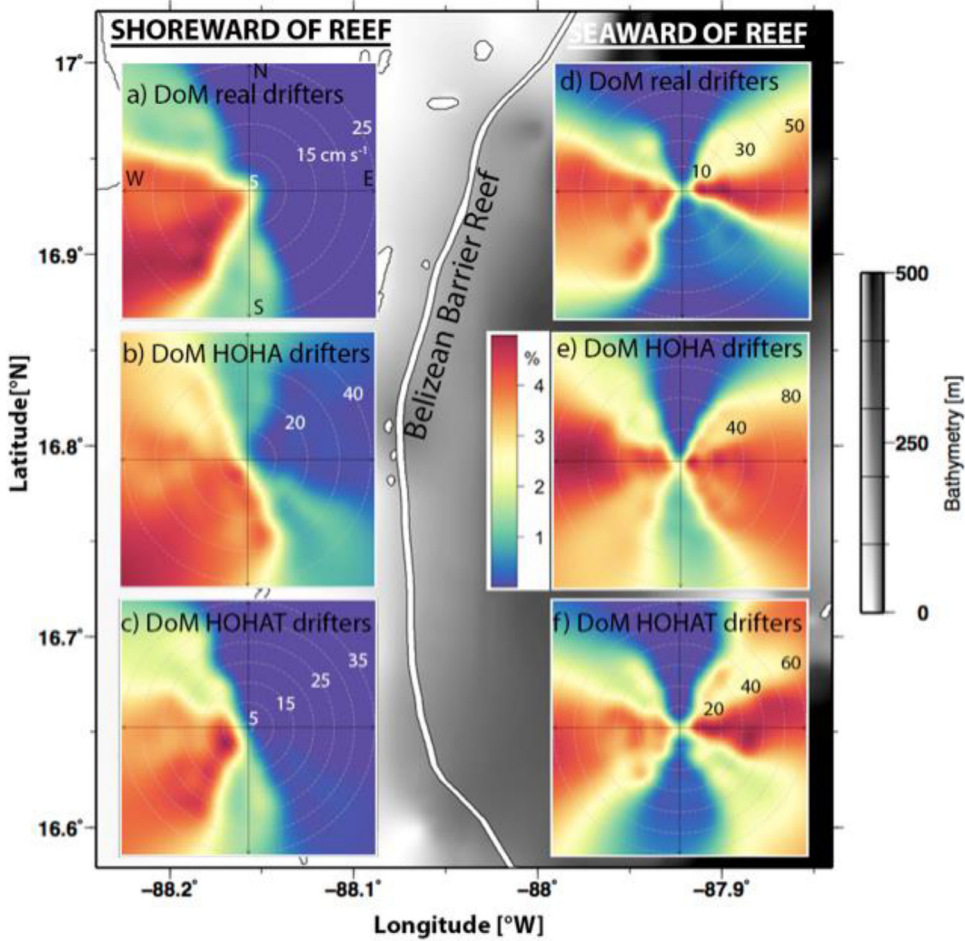


Fig. 10. Bivariate polar plots of percentage of drifters using the mean Direction of Motion (DoM) and mean speed [cm s^{-1}] for (a and d) real drifters deployed shoreward and seaward of the reef, (b and e) synthetic drifters simulated with HOHA shoreward and seaward of the reef, (c and f) synthetic drifters simulated with HOHAT shoreward and seaward of the reef.

clonic in May to an anticyclonic in August (Fig. 14a-d). SSHA is higher in the lagoon than in open waters (Fig. 14a, b) and also higher in the southern lagoon (Fig. 14b) than in the northern lagoon (Fig. 14a). Remarkably, there is a regular occurrence of sub-mesoscale cyclonic eddies at horizontal scales of $\sim 5 \text{ km}$ (Fig. 14c, d), which are smaller than one-tenth the first-baroclinic Rossby radius of deformation in the region ($\sim 6.5 \text{ km}$). The first sub-mesoscale eddy is detected along transect 88°W at 17.05°N from 20 June to 5 July (Fig. 14c, black oval), located approximately 5 km east of Columbus Island. The second sub-mesoscale eddy is detected along transect 87.55°W at 17.15°N from 12 May to 20 May (Fig. 11d, black oval), located approximately 5 km south of the southern tip of Lighthouse Atoll.

We further evaluate the role of the anticyclonic circulation around Glover's Atoll and the presence of sub-mesoscale eddies near Atolls. The high-resolution ocean-atmosphere model with tidal forcing is used by the CMS to simulate trajectories for 4-months dispersal of 100 drifters released at each of the 55 locations where in situ drifters are deployed (Fig. 15). This simulation shows how the previously discussed mesoscale circulation around Grovers Reef entrains surface particles (Fig. 15a). Particles are retained in sub-mesoscale ocean features, for example near the BBR, the southern tip of Turneffe Atoll, and in the leeward side of Glover's Atoll (red trajectories on Fig. 15b). This Lagrangian analysis provides an initial insight into the most likely pathways and retention sites after 4 months for drifters released at each of the 55 locations where in situ drifters were deployed for less than 5 h.

4. Discussions

A hierarchy of ocean-atmosphere model configurations is implemented for the BBR. To establish the most accurate model configuration and describe the ocean circulation in the BBR, we performed a Lagrangian evaluation of the models using surface drifters pairs. This investigation provides new insight into the performance of different model configurations beyond traditional Eulerian comparisons and new understanding of the sub-mesoscale flow along the BBR.

Based on the motion and speed of the drifters two interesting flow characteristics emerge. First, shoreward of the reef, drifters predominantly describe a westward motion with low variability of speeds. Second, seaward of the reef, drifters describe motions that vary counterclockwise from northeast to west with high variability of speeds. These two patterns indicate that remarkably distinct dynamics are governing surface transport seaward and shoreward of the BBR. First, flood tidal forcing seems to be leading the westward surface transport shoreward of the reef. This is supported by simulations performed with HOHA and HOHAT, because HOHAT predicts more accurately the meridional and zonal velocities both shoreward and seaward of the reef. This observation corroborates that, despite their relatively small amplitude in the BBR ($\sim 10 \text{ cm}$ amplitude), tides can excite significant high frequency flows near the reef (Ezer et al., 2011). Second, westward diurnal wind forcing, caused by the increasing temperature differences between the land and water during the day, seems to be leading to westward sur-

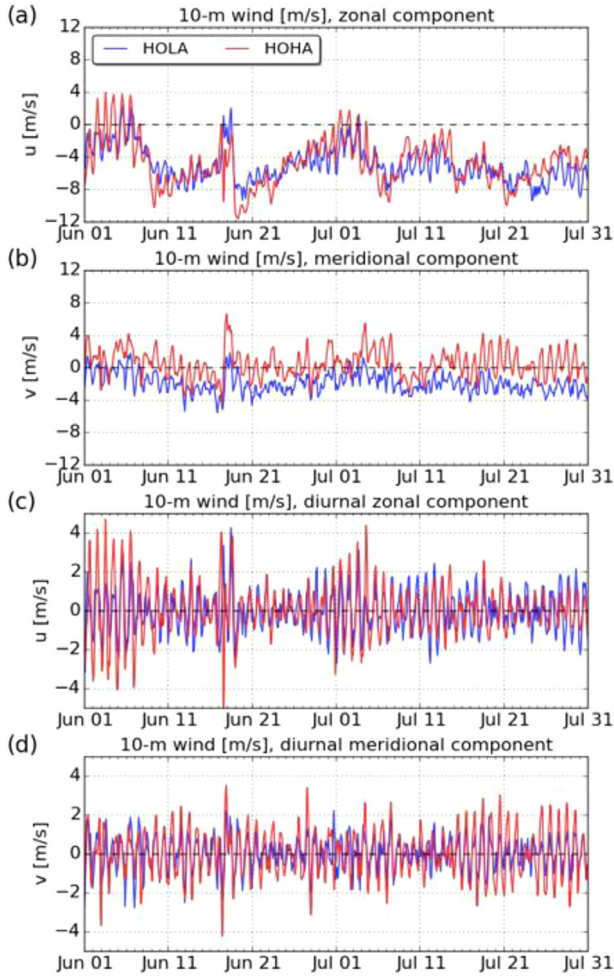


Fig. 11. Time series of (a, c) zonal and (b, d) meridional components 10-m wind averaged over the BBR domain, in case of (a, b) full velocity and (c, d) diurnal component, from experiments HOLA (blue) and HOHA (red). (For interpretation of the references to colour in this figure legend, the reader is referred to the web version of this article.)

face transport shoreward of the reef. Third, the higher variability in the direction of surface transport seaward of the reef indicates that competing mechanisms of offshore energetic mesoscale flows (Ezer et al., 2005) and sub-mesoscale local eddies genesis (this work) are causing surface transport to be more variable seaward of the reef. This contrast between transport seaward and shoreward of the reef also confirms that, unlike many shallow coastal areas, the currents seaward of the reef are not only wind driven (Armstrong, 2004; Heyman et al., 2008). The cause of these flows is likely the vertical motion of isotherms due to divergence and convergence when the mean flow interacts with topography; these variations generate internal waves that in turn generate turbulence when interacting with bottom topography (Legg and Adcroft, 2003).

We also find patterns of relative dispersion D^2 that vary geographically across the reef. Surface dispersion seaward of the reef is significantly larger than that shoreward of the reef. This is consistent with similar findings of Tang et al. (2006), who found higher dispersion seaward of Lighthouse Atoll and Glover's Atoll and lower dispersion in the inner channel shoreward of the reef near South Water Caye. The steeper and more complex bathymetry seaward of the reef might again be playing a key role, this time by increasing relative dispersion seaward of the reef. This increase of relative dispersion seaward of the reef has also been found in two regions of the southern Great Barrier Reef (GBR), where dispersion

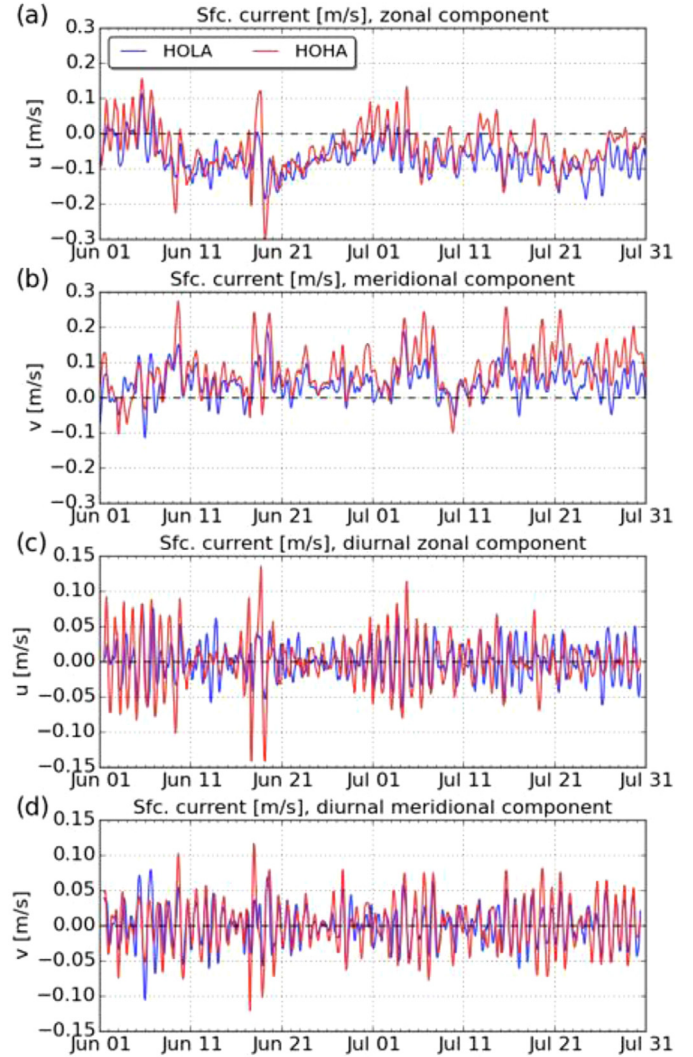


Fig. 12. Same as Fig. 11, except for surface current.

was 182 times greater along the reef than that found in the lagoon (Mantovanelli et al., 2012). These authors found that sub-mesoscale processes were important in the southern GBR, particularly in areas with complex topography where secondary circulations around the reefs and regions of steep bathymetry caused abrupt increase in dispersion. Regarding the regimes of dispersion, we observed that during the late period (180–220 min) mean D^2 increases exponentially with e-folding time of 24 min. Similar exponential increase of D^2 is observed by Ohlmann et al. (2012) during an analysis of 48 h of drifter dispersion. Information on relative dispersion on such short time scales complements the comprehensive study on surface ocean dynamics on spatial scales starting at 100 m to 100 km provided by Poje et al. (2014).

With this work we contribute to the valuable efforts that were made in the past to describe the ocean circulation in the western Caribbean Sea (Sheng and Tang, 2003), the influence of the Caribbean Current, eddies, and river runoff on the flow along the BBRS (Ezer et al., 2005; Chérubin et al., 2008), the ocean circulation and dispersion of surface waters on the Belizean shelf (Tang et al., 2006), and the flow variability in the vicinity of the reef (Paris and Chérubin, 2008; Ezer et al., 2011). Except for the 50 m resolution model of Ezer et al. (2011) on a 5 km × 5 km domain, one of the improvements here is the horizontal resolution in ocean models. The spatial and temporal resolution of the highest res-

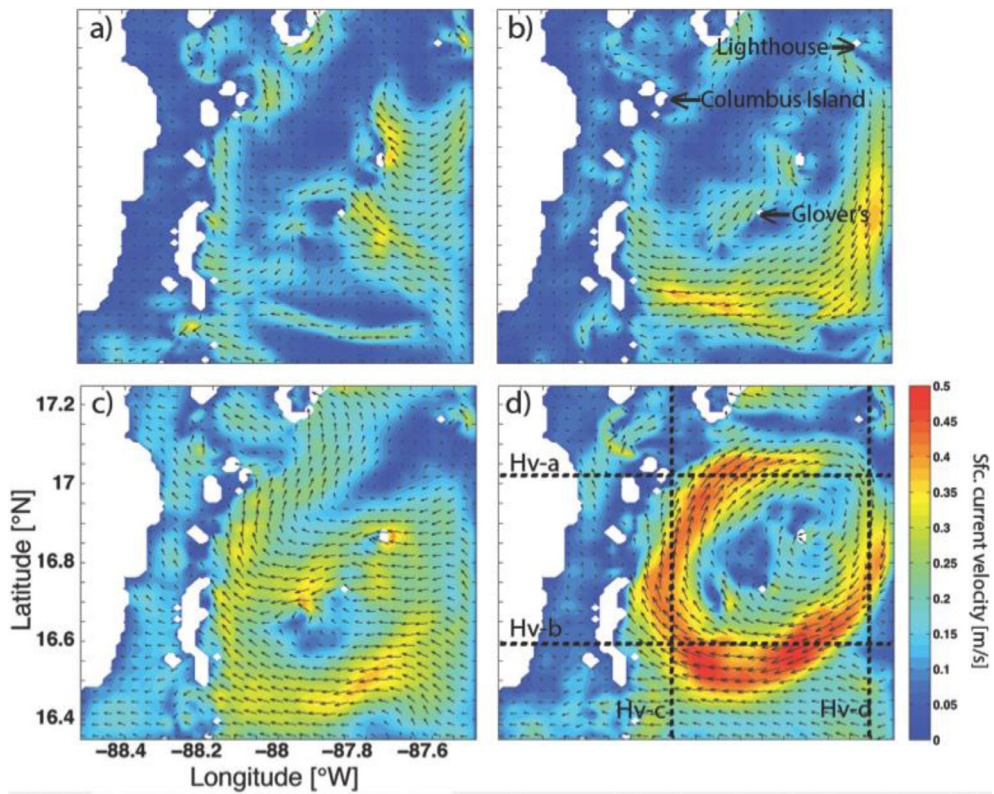


Fig. 13. Monthly surface current velocity fields from HOHAT during (a) May, (b) June, (c) July, and (d) August. Dotted lines on panels (d) at 17.1°N, 16.65°N, 88°W, and 87.55°W indicate transects used to calculate Hovmöller diagrams Hv-a, Hv-b, Hv-c, and Hv-d of Fig. 8.

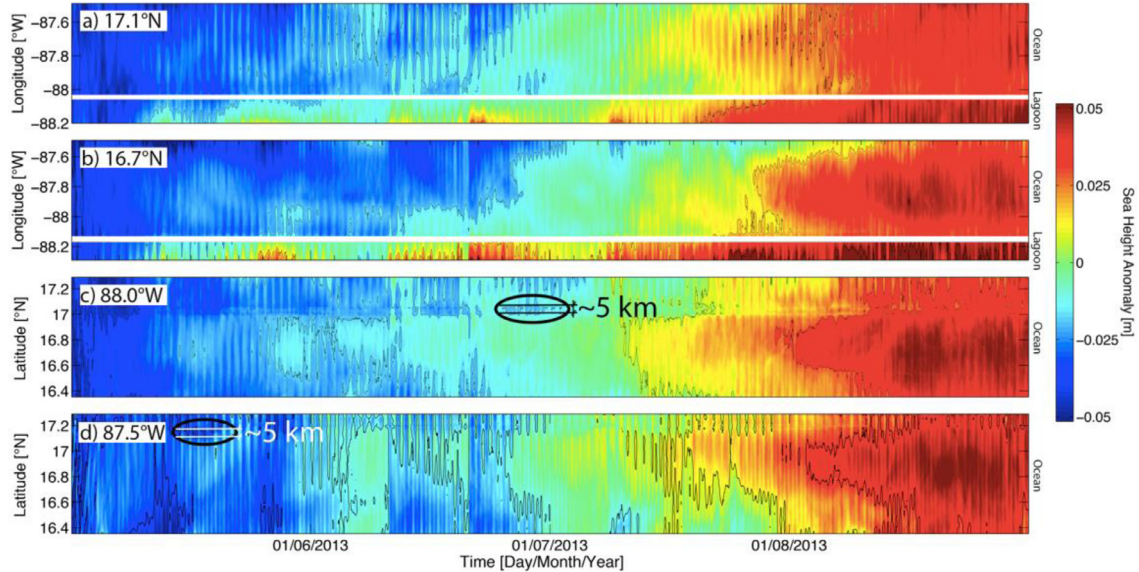


Fig. 14. Hovmöller diagrams illustrating spatial and temporal variability of sea surface height anomaly along transects at 17.1°N (a), 16.65°N (b), 88°W (c), and 87.55°W (d) (shown in Fig. 8) from 1 May to 31 August 2013. Black ovals highlight potential sub-mesoscale cyclonic eddies and approximate horizontal scales. White horizontal lines on panels (a) and (b) denote land location on the Belizean Barrier Reef.

olution atmosphere model and the resolution of the bathymetry are higher than that of all previous ocean models downscaled in the region. We think that it is important for high-resolution ocean models to also increase the resolution of both the bottom and surface boundaries.

Our analyses indicate that predictions of ocean velocity components and relative dispersion are highly sensitive to changes in spatial-temporal resolution of ocean-atmosphere model output.

Because we increased both spatial and temporal resolution, we cannot assess whether improvements in velocity components and relative dispersion are most influenced by increase in temporal or spatial resolution. This is a new line of research to be explored in future studies. Unlike lower resolution models, BBR-HYCOM is providing Lagrangian trajectories for all the shallow locations where real drifters are deployed. This is indispensable to understand the coastal transport and mixing processes in the BBR. All

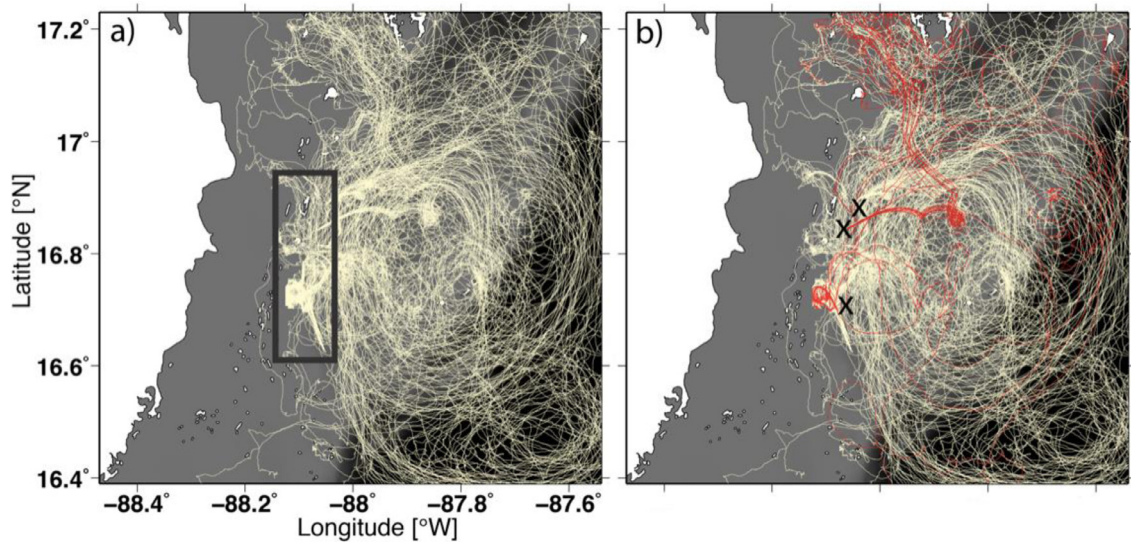


Fig. 15. (a) Simulated trajectories of 100 drifters released at each of the same locations where in situ drifters were deployed (black rectangle), and (b) examples of simulated trajectories of 100 drifters released in three specific locations where in situ drifters were deployed (black cross) for 4 months of high-resolution dispersal with HOHAT, from 1 May to 31 August 2013. (For interpretation of the references to colour in the text, the reader is referred to the web version of this article.)

model configurations of BBR-HYCOM provide quantifiable agreement between u and v velocities of drifters and u and v velocities of Lagrangian particles, with discrepancies smaller than 0.05 m s^{-1} for u and differences smaller than 0.16 m s^{-1} for v . Increasing the spatial-temporal resolution of the ocean models increases the accuracy on u , v . Numerical discrepancies for u and v are reduced by 30% and 13% respectively. Incorporating tidal forcing to the high-resolution ocean-atmosphere model increases the accuracy on u and v . Numerical discrepancies for u and v are reduced by 64% and 67% respectively. The use of high frequency atmospheric forcing is likely to change more dramatically the vertical mixing by exciting quasi- and near inertial waves as a geostrophic expression of the mesoscale eddy field (Cardona and Bracco, 2014), and may potentially influence the density structure of the water column. We evaluated the wind forcing from the HOLA and HOHA, and compared the resulting ocean currents response. HOHA has statistically more realistic small-scale processes and increased variability on diurnal time scales.

Relative dispersion is accurately reproduced by all the configurations of BBR-HYCOM, but statistically significant differences are found in relative dispersion between all model configurations. For the short temporal and spatial scales of this study the model configuration that maximizes agreement between observed and modeled relative dispersion is the high-resolution ocean and high-resolution atmospheric model with tidal forcing (HOHAT). Because LOLA barely resolves the mesoscale eddies and HOLA resolves the sub-mesoscale eddies, the circulation resolved by LOLA is not able to trap Lagrangian particles like HOLA. Increasing the horizontal and temporal resolution of the ocean model reduced the D^2 numerical discrepancies by approximately 68%, and incorporating tidal forcing further reduce the D^2 numerical discrepancies by approximately 30%.

Model validation from available observations in the region helps to evaluate surface transport predictions from LOLA, HOLA, HOHA, and HOHAT. We validated the wind predictions from HOLA and HOHA against observations from a meteorological station. The overall synoptic patterns are better represented by HOLA, but HOHA better resolves the diurnal variability and is more capable of capturing the local maxima in both zonal and meridional directions. We validated the sea surface temperatures from LOLA, HOLA,

HOHA, and HOHAT against observations from two meteorological stations, and provide a qualitative example of ability of the models to synoptically represent the mesoscale SST patterns. HOLA, HOHA, and HOHAT predict SST significantly better than LOLA, however all four models have a positive bias. While LOLA show SST anomalies greater than 1.5°C , HOLA, HOHA, and HOHAT show SST anomalies less than 0.9°C . Model derived SST from HOLA, HOHA, and HOHAT are consistent with the strong zonal gradient of SST.

The improved performance of HOHA and HOHAT in predicting surface velocities and dispersion can be due to the fact that both high-resolution ocean models are resolving more mesoscale and sub-mesoscale looping trajectories. While HOLA is resolving a 10% of looping trajectories, HOHA and HOHAT are resolving a 21% and 29% of looping trajectories, respectively. The optimal performance of HOHAT in predicting surface velocities and dispersion can be due to the fact that, unlike the other models, most of the looping trajectories that HOHAT is resolving (21% out of 29%) are in the sub-mesoscale range, which play a critical role in particle dispersion of the short scales of this investigation.

Because incorporating tidal forcing further reduces discrepancies in velocity and relative dispersion, and resolves the highest percentage of looping drifters, the model configuration that maximizes agreement between observed and modeled u and v velocities is the high-resolution ocean and high-resolution atmospheric model with tidal forcing (HOHAT).

The spatial-temporal variability in the ocean circulation is described using HOHAT and a Lagrangian approach. Model output using HOHAT indicates that; (1) the magnitude of surface current velocities intensifies throughout the summer and peaks in August 2013; (2) mesoscale anticyclonic circulation is formed around Grovers Reef in August 2013; and (3) sub-mesoscale ocean features are formed in the vicinity of Columbus Island and between the BBR and the southern tip of Glover's Atoll. A final Lagrangian analysis shows the most likely pathways on the previously mentioned anticyclonic circulation feature and retention sites in sub-mesoscale ocean feature for drifters released at each of the 55 locations where in situ drifters were deployed. To the best of our knowledge this is the first time that sub-mesoscale eddies are reported in the region.

5. Summary

In summary, we have constructed a hierarchy of ocean-atmosphere model configurations that reproduce the rapid changes in surface transport induced by a very steep bathymetry near the reef and by atmospheric forcing on shallow waters along the BBR. The BBR-HYCOM represents accurately small-scale dispersion, which is important for a wide range of applications, from modeling reef-fish larval dispersal to the transport of pollutants. Explicitly, we have shown that increasing the spatial and temporal resolution of the ocean model ($1/12^\circ$ to $1/100^\circ$ and 24 h to 1 h) and that of the atmosphere model ($1/2^\circ$ versus $1/100^\circ$ and 6 h to 1 h), reduce discrepancy between simulated and observed relative dispersion and velocity components. Moreover, introducing tidal forcing to the highest ocean-atmosphere model configuration reduces discrepancy between simulated and observed velocity components. Although the impacts of increasing the resolution of ocean models on model outputs have been tested at basin-scale (e.g., Hurlbert and Hogan, 2000; Wei et al., 2013) the number of works that test model outputs with drifters on a barrier reef system is very low (Condie and Andrewartha, 2008). Further, the impact of high-resolution atmosphere forcing on ocean model outputs has not been tested to date. Our improvements in surface transport prediction complement previous modeling efforts in the region (Sheng and Tang, 2003; Ezer et al., 2005; Tang et al., 2006; Chérubin et al., 2008; Ezer et al., 2011) and suggest that Lagrangian evaluation should become systematic in the development of coastal models geared for biophysical applications.

The main advances of this study are that it provides: 1) a general framework to estimate the best surface transport prediction from different ocean-atmosphere models using metrics derived from accurate high frequency drifters' data and data from available meteorological stations; and 2) a high-resolution ocean-atmosphere model that shows consistency of the expected velocities and dispersion with in situ drifters deployed in shallow lagoons, steep walls, and oceanic waters of the Belizean Barrier Reef on scales of hours. Accurate predictions of such short time scales are important because they might determine the total distance that larval-fish disperse. This work lays the foundation for better understanding the patterns of larval dispersal and population connectivity being revealed by genetic analyses in the area.

Acknowledgments

This research is supported by the National Science Foundation award **NSF-OCE 1260424**. We thank CARTHE Consortium for providing the Lagrangian drifters; the Center for Computational Science (CCS) of the University of Miami for operational support with multi-processors; Kevin David, Alben David, Ashford Velasquez, Cédric Guigand, and the staff of International Zoological Expeditions for logistical support in the field. Research permission was granted by Belize Fisheries. We acknowledge the contributions of two anonymous reviewers who helped improve the manuscript.

References

- Almany, G.R., Connolly, S.R., Heath, D.D., Hogan, J.D., Jones, G.P., McCook, L.J., Mills, M., Pressey, R.L., Williamson, D.H., 2009. Connectivity, biodiversity conservation and the design of marine reserve networks for coral reefs. *Coral Reefs* 28 (2), 339–351.
- Anderson, M.J., 2001. A new method for non-parametric multivariate analysis of variance. *Aust. J. Ecol.* 26 (1), 32–46.
- Andréfouët, S., Müller-Karger, F.E., Robinson, J.A., Kranenburg, C.J., Torres-Pulliza, D., Spraggins, S.A., Murch, B., 2006. Global assessment of modern coral reef extent and diversity for regional science and management applications: a view from space. In: *Proceedings of the 10th International Coral Reef Symposium*, 2, pp. 1732–1745.
- Arbic, B.K., Richman, J.G., Shriner, J.F., Timko, P.G., Metzger, E.J., Wallcraft, A.J., 2012. Global Modeling of Internal Tides within an Eddying Ocean General Circulation Model. DTIC Document.
- Arbic, B.K., Wallcraft, A.J., Metzger, E.J., 2010. Concurrent simulation of the eddying general circulation and tides in a global ocean model. *Ocean Model.* 32, 175–187.
- Armstrong, B.N., 2004. Currents along the Mesoamerican Barrier Reef, Western Caribbean. In: *AGU Fall Meeting Abstracts*, 1, p. 0504.
- Bleck, R., 2002. An oceanic general circulation model framed in hybrid isopycnic-Cartesian coordinates. *Ocean Model.* 4 (1), 55–88.
- Brankart, J.M., 2013. Impact of uncertainties in the horizontal density gradient upon low resolution global ocean modelling. *Ocean Model.* 66, 64–76.
- Buijsman, M.C., Arbic, B.K., Green, J.A.M., Helber, R.W., Richman, J.G., Shriner, J.F., Timko, P.G., Wallcraft, A., 2015. Optimizing internal wave drag in a forward barotropic model with semidiurnal tides. *Ocean Model.* 85, 42–55.
- Cardona, Y., Bracco, A., 2014. Predictability of mesoscale circulation throughout the water column in the Gulf of Mexico. *Deep Sea Res. Pt. II: Top. Stud. Oceanogr.* 129, 332–349.
- Carrillo, L., Johns, E.M., Smith, R.H., Lamkin, J.T., Largier, J.L., 2015. Pathways and hydrography in the Mesoamerican Barrier Reef System part 1: circulation. *Cont. Shelf Res.* 109, 164–176.
- Carslaw, D.C., Ropkins, K., 2012. Openair—an R package for air quality data analysis. *Environ. Model. Softw.* 27, 52–61.
- Carter, G.S., Fringer, O.B., Zaron, E.D., 2012. Regional Models of Internal Tides.
- Chassignet, E.P., Smith, L.T., Halliwell, G.R., Bleck, R., 2003. North Atlantic simulations with the Hybrid Coordinate Ocean Model (HYCOM): impact of the vertical coordinate choice, reference pressure, and thermobaricity. *J. Phys. Oceanogr.* 33 (12), 2504–2526.
- Chelton, D.B., Deszoeke, R.A., Schlax, M.G., El Naggar, K., Siwertz, N., 1998. Geographical variability of the first baroclinic Rossby radius of deformation. *J. Phys. Oceanogr.* 28 (3), 433–460.
- Chérubin, L.M., Kuchinke, C.P., Paris, C.B., 2008. Ocean circulation and terrestrial runoff dynamics in the Mesoamerican region from spectral optimization of SeaWiFS data and a high resolution simulation. *Coral Reefs* 27 (3), 503–519.
- Cho, L., 2005. Marine protected areas: a tool for integrated coastal management in Belize. *Ocean Coast. Manage.* 48 (11), 932–947.
- Cisneros-Montemayor, A.M., Kirkwood, F.G., Harper, S., Zeller, D., Sumaila, U.R., 2013. Economic use value of the Belize marine ecosystem: potential risks and benefits from offshore oil exploration. *Nat. Resour. Forum* 37 (4), 221–230.
- Clarke, K.R., Gorley, R.N., 2006. PRIMER v6, User Manual/Tutorial. Plymouth Routine in Multivariate Ecological Research. Plymouth Marine Laboratory.
- Condie, S.A., Andrewartha, J.R., 2008. Circulation and connectivity on the Australian North West shelf. *Cont. Shelf Res.* 28 (14), 1724–1739.
- Cooper, E., Burke, L., Bood, N., 2009. Coastal capital: Belize. In: *The Economic Contribution of Belize's Coral Reefs and Mangroves*. World Resources Institute, Washington, DC, USA, p. 54.
- Cummings, J.A., 2005. Operational multivariate ocean data assimilation. *Q. J. R. Meteorol. Soc.* 131 (613), 3583–3604.
- Curcic, M., Chen, S.S., Özgökmen, T.M., 2016. Hurricane-induced ocean waves and Stokes drift and their impacts on surface transport and dispersion in the Gulf of Mexico. *Geophys. Res. Lett.* 43, 2773–2781. doi:10.1002/2015GL067619.
- D'Aloia, C.C., Bogdanowicz, S.M., Francis, R.K., Majoris, J.E., Harrison, R.G., Buston, P.M., 2015. Patterns, causes, and consequences of marine larval dispersal. *Proc. Natl. Acad. Sci.* 112 (45), 13940–13945.
- D'Aloia, C.C., Bogdanowicz, S.M., Harrison, R.G., Buston, P.M., 2014. Seascape continuity plays an important role in determining patterns of spatial genetic structure in a coral reef fish. *Mol. Ecol.* 23, 2902–2913.
- D'Aloia, C.C., Bogdanowicz, S.M., Majoris, J.E., Harrison, R.G., Buston, P.M., 2013. Self-recruitment in a Caribbean reef fish: a method for approximating dispersal kernels accounting for seascape. *Mol. Ecol.* 22 (9), 2563–2572.
- Donelan, M.A., Haus, B.K., Reul, N., Plant, W.J., Stiassnie, M., Gruber, H.C., Brown, O.B., Saltzman, E.S., 2004. On the limiting aerodynamic roughness of the ocean in very strong winds. *Geophys. Res. Lett.* 31, L18306.
- Ezer, T., Arango, H., Shchepetkin, A.F., 2002. Developments in terrain-following ocean models: intercomparisons of numerical aspects. *Ocean Model.* 4, 249–267. doi:10.1016/S1463-5003(02)00003-3.
- Ezer, T., Heyman, W.D., Houser, C., Kjerfve, B., 2011. Modeling and observations of high-frequency flow variability and internal waves at a Caribbean reef spawning aggregation site. *Ocean Dynam.* 61 (5), 581–598.
- Ezer, T., Heyman, W.D., Houser, C., Kjerfve, B., 2012. Extreme flows and unusual water levels near a Caribbean coral reef: was this a case of a "perfect storm"? *Ocean Dynam.* 62 (7), 1043–1057.
- Ezer, T., Thattai, D.V., Kjerfve, B., Heyman, W.D., 2005. On the variability of the flow along the Meso-American Barrier Reef system: a numerical model study of the influence of the Caribbean current and eddies. *Ocean Dynam.* 55 (5–6), 458–475.
- Fogarty, M.J., Botsford, L.W., 2007. Population connectivity. *Oceanography* 20 (3), 112.
- Garner, S.T., 2005. A topographic drag closure built on an analytical base flux. *J. Atmos. Sci.* 62, 2302–2315.
- Graham, D.I., Moyeed, R.A., 2002. How many particles for my Lagrangian simulations? *Powder Technol.* 125.2, 179–186.
- Griffa, A., 1996. Applications of stochastic particle models to oceanographic problems. In: *Stochastic Modelling in Physical Oceanography*. Birkhäuser Boston, pp. 113–140.
- Griffies, S.M., Gnanadesikan, A., Dixon, K.W., Dunne, J.P., Gerdes, R., Harrison, M.J., Rosati, A., Russell, J.L., Samuels, B.L., Spelman, M.J., 2005. Formulation of an ocean model for global climate simulations. *Ocean Sci.* 1 (1812–0784), 45–79.

- Heyman, W.D., Kjerfve, B., Ezer, T., 2008. Mesoamerican reef spawning aggregations help maintain fish populations: a review of connectivity research and priorities for science and management. In: Caribbean Connectivity: Implications for Marine Protected Area Management, pp. 150–169.
- Hogan, T.F., Rosmond, T.E., 1991. The description of the Navy Operational Global Atmospheric Prediction System's spectral forecast model. *Mon. Weather Rev.* 119 (8), 1786–1815.
- Hong, S.Y., Dudhia, J., Chen, S.H., 2004. A revised approach to ice microphysical processes for the bulk parameterization of clouds and precipitation. *Mon. Weather Rev.* 132 (1), 103–120.
- Hong, S.-Y., Noh, Y., Dudhia, J., 2006. A new vertical diffusion package with an explicit treatment of entrainment processes. *Mon. Weather Rev.* 134 (9), 2318–2341.
- Hurlbert, H.E., Hogan, P.J., 2000. Impact of 1/8 to 1/64 resolution on Gulf Stream model—data comparisons in basin-scale subtropical Atlantic Ocean models. *Dyn. Atmos. Oceans* 32 (3), 283–329.
- Judt, F., Chen, S.S., Curcic, M., 2016. Atmospheric forcing on the upper ocean transport in the Gulf of Mexico: from seasonal to diurnal time scales. *J. Geophys. Res. Oceans* 121, 4416–4433. doi:10.1002/2015JC011555.
- Karnauskas, M., Cherubin, L.M., Huntington, B.E., Babcock, E.A., Thoney, D.A., 2012. Physical forces influence the trophic structure of reef fish communities on a remote atoll. *Limnol. Oceanogr.* 57 (5), 1403–1414.
- Klocker, A., McDougall, T.J., 2010. Influence of the nonlinear equation of state on global estimates of dianeutral advection and diffusion. *J. Phys. Oceanogr.* 40 (8), 1690–1709.
- LaCasce, J.H., 2008. Statistics from Lagrangian observations. *Prog. Oceanogr.* 77 (1), 1–29.
- Large, W.G., McWilliams, J.C., Doney, S.C., 1994. Oceanic vertical mixing: a review and a model with a nonlocal boundary layer parameterization. *Rev. Geophys.* 32 (4), 363–403.
- Legg, S., Adcroft, A., 2003. Internal wave breaking at concave and convex continental slopes. *J. Phys. Oceanogr.* 33 (11), 2224–2246.
- Leichter, J.J., Stewart, H.L., Miller, S.L., 2003. Episodic nutrient transport to Florida coral reefs. *Limnol. Oceanogr.* 48, 1394–1407.
- Lindo-Atchati, D., P., Sangrà, 2015. Observational evidence for atmospheric modulation of the Loop Current migrations. *Front. Earth Sci.* 9 (4), 683–690.
- Luettich, R.A. Jr., Westerink, J.J., & Scheffner, N.W. (1992). ADCIRC: An Advanced Three-Dimensional Circulation Model for Shelves, Coasts, and Estuaries. Report 1. Theory and Methodology of ADCIRC-2DDI and ADCIRC-3DL (No. CERC-TR-DRP-92-6). Coastal Engineering Research Center, Vicksburg, MS.
- Lynch, D.R., Greenberg, D.A., Bilgili, A., McGillicuddy Jr., D.J., Manning, J.P., Aretxabaleta, A.J., 2014. Particles in the Coastal Ocean: Theory and Applications. Cambridge University Press.
- MacMahan, J., Brown, J., Thornton, E., 2009. Low-cost handheld global positioning system for measuring surf-zone currents. *J. Coastal Res.* 25, 744–754.
- Manning, J.P., Churchill, J.H., 2006. Estimates of dispersion from clustered-drifter deployments on the southern flank of Georges Bank. *Deep Sea Res. Pt. II: Top. Stud. Oceanogr.* 53 (23), 2501–2519.
- Mantovanelli, A., Heron, M.L., Heron, S.F., Steinberg, C.R., 2012. Relative dispersion of surface drifters in a barrier reef region. *J. Geophys. Res.: Oceans* 117 (C11), 1–15.
- McClanahan, T., Karnauskas, M., 2011. Relationships between benthic cover, current strength, herbivory, and a fisheries closure in Grovers Reef Atoll, Belize. *Coral Reefs* 30 (1), 9–19.
- Mensa, J.A., Özgökmen, T.M., Poje, A.C., Imberger, J., 2015. Material transport in a convective surface mixed layer under weak wind forcing. *Ocean Model.* 96, 226–242.
- Monin, A.S., Obukhov, A., 1954. Basic laws of turbulent mixing in the surface layer of the atmosphere. *Contrib. Geophys. Inst. Acad. Sci. USSR* 151, 163–187.
- Mariano, A.J., Griffa, A., Özgökmen, T.M., Zambianchi, E., 2002. Lagrangian analysis and predictability of coastal and ocean dynamics 2000. *Journal of Atmospheric and Oceanic Technology* 19 (7), 1114–1126.
- Ohlmann, J., LaCasce, J.H., Washburn, L., Mariano, A.J., Emery, B., 2012. Relative dispersion observations and trajectory modeling in the Santa Barbara Channel. *J. Geophys. Res.* 117 (C5), 1–14.
- Okubo, A., 1971. Oceanic Diffusion Diagrams. Elsevier.
- Paris, C.B., Chérubin, L.M., 2008. River-reef connectivity in the Mesoamerican Barrier Reef. *Coral Reefs* 27 (4), 773–781.
- Paris, C.B., Chérubin, L.M., Cowen, R.K., 2007. Surfing, spinning, or diving from reef to reef: effects on population connectivity. *Mar. Ecol. Prog. Ser.* 347, 285–300.
- Paris, C.B., Cowen, R.K., Lwiza, K.M.M., Wang, D.P., Olson, D.B., 2002. Objective analysis of three-dimensional circulation in the vicinity of Barbados, West Indies: implication for larval transport. *Deep Sea Res.* 49, 1363–1386.
- Paris, C.B., Helgers, J., van Sebille, E., Srinivas, A., 2013. Connectivity modeling system: a probabilistic modeling tool for the multi-scale tracking of biotic and abiotic variability in the ocean. *Environ. Model. Soft.* 42, 47–54.
- Pauly, D., Hilborn, R., Branch, T.A., 2013. Fisheries: does catch reflect abundance? *Nature* 494 (7437), 303–306.
- PiNeda, J., Hare, J.A., Sponaugle, S., 2007. Larval Transport and Dispersal in the Coastal Ocean and Consequences for Population Connectivity.
- Poje, A.C., Özgökmen, T.M., Lippardt, B.L., Haus, B.K., Ryan, E.H., Haza, A.C., Jacobs, G.A., Reniers, A., Olascoaga, M.J., Novelli, G., 2014. Sub-mesoscale dispersion in the vicinity of the Deepwater Horizon spill. *Proc. Natl. Acad. Sci.* 111 (35), 12693–12698.
- Qin, X., van Sebille, E., Sen Gupta, A., 2014. Quantification of errors induced by temporal resolution on Lagrangian particles in an eddy-resolving model. *Ocean Model.* 76, 20–30.
- Rainville, L., Pinkel, R., 2006. Propagation of low-mode internal waves through the ocean. *J. Phys. Oceanogr.* 36 (6), 1220–1236.
- Richardson, L.F., 1926. Atmospheric diffusion shown on a distance-neighbour graph. *Proc. R. Soc. London. Ser. A, Containing Papers Math. Phys. Character* 110 (756), 709–737.
- Richardson, P.L., 1993. A census of eddies observed in North Atlantic SOFAR float data. *Prog. Oceanogr.* 31 (1), 1–50.
- Sala, E., Aburto-Oropeza, O., Paredes, G., Parra, I., Barrera, J.C., Dayton, P.K., 2002. A general model for designing networks of marine reserves. *Science* 298 (5600), 1991–1993.
- Schroeder, K., Haza, A.C., Griffa, A., Özgökmen, T.M., Poulain, P.M., Gerin, R., Rixen, M., 2011. Relative dispersion in the Liguro-Provençal basin: From sub-mesoscale to mesoscale. *Deep Sea Res. Pt. I: Oceanogr. Res. Papers* 58 (3), 209–228.
- Schepetkin, A.F., McWilliams, J.C., 2005. The regional oceanic modeling system (ROMS): a split-explicit, free-surface, topography-following-coordinate oceanic model. *Ocean Model.* 9 (4), 347–404.
- Shcherbinina, A.Y., Gawarkiewicz, G.G., Linder, C.A., Thorrold, S.R., 2008. Mapping bathymetric and hydrographic features of Glover's Reef, Belize, with a REMUS autonomous underwater vehicle. *Limnol. Oceanogr.* 53 (5), 2264.
- Sheng, J., Tang, L., 2003. A numerical study of circulation in the western Caribbean Sea. *J. Phys. Oceanogr.* 33 (10), 2049–2069.
- Shriver, J.F., Arbic, B.K., Richman, J.G., Ray, R.D., Metzger, E.J., Wallcraft, A.J., Timko, P.G., 2012. An evaluation of the barotropic and internal tides in a high-resolution global ocean circulation model. *J. Geophys. Res. Oceans* 117, 1–14.
- Skamarock, W.C., Klemp, J.B., 2008. A time-split nonhydrostatic atmospheric model for weather research and forecasting applications. *J. Comput. Phys.* 227 (7), 3465–3485.
- Snyder, R.E., Paris, C.B., Vaz, A.C., 2014. How much do marine connectivity fluctuations matter? *Am. Nat.* 184 (4), 523–530.
- Soto, I., Andréfouët, S., Hu, C., Müller-Karger, F.E., Wall, C.C., Sheng, J., Hatcher, B.G., 2009. Physical connectivity in the Mesoamerican Barrier Reef System inferred from 9 years of ocean color observations. *Coral Reefs* 28 (2), 415–425.
- Stammer, D., Ray, R.D., Andersen, O.B., Arbic, B.K., Bosch, W., Carrère, L., Cheng, Y., Chin, D.S., Dushaw, B.D., Egbert, G.D., 2014. Accuracy assessment of global barotropic ocean tide models. *Rev. Geophys.* 52, 243–282.
- Tang, L., Sheng, J., Hatcher, B.G., Sale, P.F., 2006. Numerical study of circulation, dispersion, and hydrodynamic connectivity of surface waters on the Belize shelf. *J. Geophys. Res.* 111 (C1), 1–18.
- Veneziani, M., Griffa, A., Garraffo, Z.D., Chassignet, E.P., 2005. Lagrangian spin parameter and coherent structures from trajectories released in a high-resolution ocean model. *J. Mar. Res.* 63 (4), 753–788.
- Veneziani, M., Griffa, A., Reynolds, A.M., Garraffo, Z.D., Chassignet, E.P., 2005. Parameterizations of Lagrangian spin statistics and particle dispersion in the presence of coherent vortices. *J. Mar. Res.* 63 (6), 1057–1083.
- Veneziani, M., Griffa, A., Reynolds, A.M., Mariano, A.J., 2004. Oceanic turbulence and stochastic models from subsurface Lagrangian data for the Northwest Atlantic Ocean. *J. Phys. Oceanogr.* 34 (8), 1884–1906.
- Wallcraft, A.J., Metzger, E.J., Carroll, S.N., 2009. Software Design Description for the HYbrid Coordinate Ocean Model (HYCOM), Version 2.2, edited, DTIC Document.
- Wei, M., Jacobs, G., Rowley, C., Barron, C.N., Hogan, P., Spence, P., Smedstad, O.M., Martin, P., Muscarella, P., Coelho, E., 2013. The performance of the US Navy's RELO ensemble, NCOM, HYCOM during the period of GLAD at-sea experiment in the Gulf of Mexico. *Deep Sea Res. Pt. II: Top. Stud. Oceanogr.* 129, 374–393.
- West, B.T., Welch, K.B., Galecki, A.T., 2006. Linear Mixed Models: A Practical Guide Using Statistical Software. CRC Press.
- Wood, S., Paris, C.B., Ridgwell, A., Hendy, E.J., 2014. Modelling dispersal and connectivity of broadcast spawning corals at the global scale. *Global Ecol. Biogeogr.* 23 (1), 1–11.